

# Online Research @ Cardiff

This is an Open Access document downloaded from ORCA, Cardiff University's institutional repository: <https://orca.cardiff.ac.uk/id/eprint/125809/>

This is the author's version of a work that was submitted to / accepted for publication.

Citation for final published version:

Ouro, Pablo, Muhawenimana, Valentine ORCID: <https://orcid.org/0000-0002-9538-2229> and Wilson, Catherine A.M.E. ORCID: <https://orcid.org/0000-0002-7128-590X> 2019. Asymmetric wake of a horizontal cylinder in close proximity to a solid boundary for Reynolds numbers in the subcritical turbulence regime. *Physical Review Fluids* 4 , 104604. 10.1103/PhysRevFluids.4.104604 file

Publishers page: <https://doi.org/10.1103/PhysRevFluids.4.104604>  
<<https://doi.org/10.1103/PhysRevFluids.4.104604>>

Please note:

Changes made as a result of publishing processes such as copy-editing, formatting and page numbers may not be reflected in this version. For the definitive version of this publication, please refer to the published source. You are advised to consult the publisher's version if you wish to cite this paper.

This version is being made available in accordance with publisher policies.

See

<http://orca.cf.ac.uk/policies.html> for usage policies. Copyright and moral rights for publications made available in ORCA are retained by the copyright holders.



**<sup>1</sup> Asymmetric wake of a horizontal cylinder in close proximity to a solid boundary for  
<sup>2</sup> Reynolds numbers in the sub-critical turbulence regime**

<sup>3</sup> Pablo Ouro,<sup>1, a)</sup> Valentine Muhawenimana,<sup>1, b)</sup> and Catherine A.M.E. Wilson<sup>1, c)</sup>

<sup>4</sup> *Hydro-environmental Research Centre, School of Engineering, Cardiff University,*  
<sup>5</sup> *UK*

<sup>6</sup> (Dated: 1 October 2019)

The near wake dynamics developed behind a horizontal cylinder with wall proximity effects are elucidated from laboratory experiments and Large-Eddy Simulations (LES). Fixed vertical gap to diameter ( $G/D$ ) ratios of 0.5 and 1.0 were investigated for Reynolds numbers equal to 6,666, 10,000 and 13,333. The LES results agreed well with the experimental measurements for the time-averaged flow quantities and captured the upward flow motion developed over the lower half of the flow depth as a consequence of the near-wall effect. The presence of a narrow gap between the cylinder and the bed, i.e.  $G/D = 0.5$ , significantly influenced the dynamics of the vortex generation and shedding which, in consequence, led to an increasingly pronounced asymmetric wake distribution with increasing Reynolds number. In the wider gap case of  $G/D = 1.0$ , the wake remained relatively symmetrical, with reduced impact of ground proximity. Kelvin-Helmholtz instabilities developed in the upper and lower shear layers were shown to be decoupled as their instantaneous laminar-to-turbulent transition occurred at different downstream distances at any given time. Spanwise rollers were shown to form with an undulating pattern and presented irregularly located vortex dislocations. Furthermore, a ground-vortex induced during the early stages of the lower roller's generation in the wake lifted off the ground and merged with the von-Kármán vortices to form a single vortical structure. For  $G/D = 0.5$ , a positive upwards force was present, and experimental and LES Strouhal number values ranged between 0.28–0.32, while computed drag coefficient values were lower than those typical for unbounded cylinder flows. As for  $G/D = 1.0$ , Strouhal numbers decrease to a 0.26–0.30 range whilst drag coefficient increases, further demonstrating the effects on the cylinder wake structure dynamics due to the proximity to a solid boundary.

7

PACS numbers: 47.32,47.27

---

<sup>a)</sup>ourop@cardiff.ac.uk

<sup>b)</sup>muhawenimanav@cardiff.ac.uk

<sup>c)</sup>wilsonca@cardiff.ac.uk

## I. INTRODUCTION

The wake structure around a vertically orientated cylinder has been the subject of research for more than a century due to the abundance of curved bodies in nature as well as in civil, mechanical and aeronautical engineering. Recent research efforts have also focused on the flow structure in the wake of a horizontal-orientated cylinder<sup>1,2</sup>, i.e. its main axis is parallel to a close wall and perpendicular to the flow direction as depicted in Fig. 1. The dependency of the wake dynamics on the Reynolds number ( $Re = UD/\nu$ ) has been studied extensively for vertical cylinders and to a lesser extent for horizontal cylinders. This knowledge is critical to our understanding of how the dynamic forces imposed by the fluid on the body change as a function of flow regime and fluid viscosity, as pertaining to fluid-body interactions.

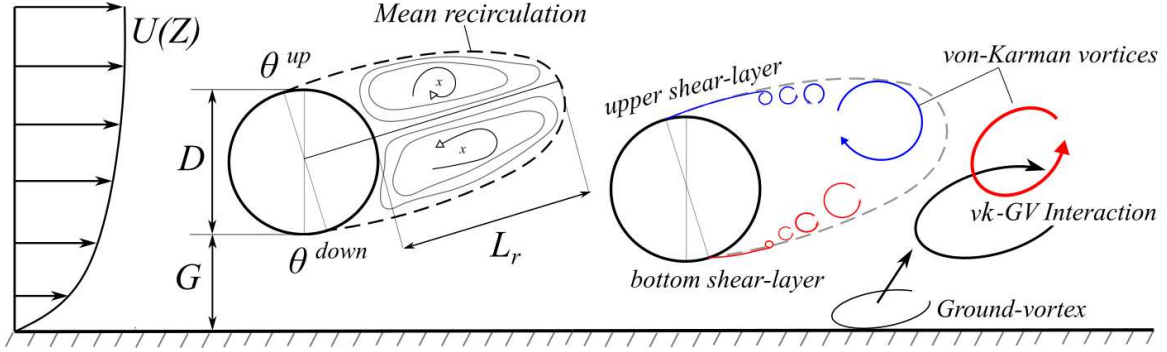


FIG. 1: Schematic of the wake dynamics in horizontal cylinder flows in proximity to a wall and with logarithmic approaching velocity profile. The main instantaneous wake dynamics phenomena, such as the Ground-Vortex (GV) or von-Kármán vortices ( $vk$ ), are depicted together with the time-averaged wake characteristics, such as recirculation length  $L_r$ , separation angles  $\theta$ .

Flow around a horizontal cylinder can exhibit different behaviour compared to a vertical cylinder, depending on the flow conditions in which is embedded, such as in a boundary layer flows<sup>1</sup>, or be influenced by its proximity to the ground<sup>2</sup>; resulting in altered wake dynamics as shown in Fig. 1. Some of these changes are related to asymmetric vortex shedding, modification of the separation angles or the appearance of a ground-vortex. This ground-vortex notably interacts with the von-Kármán vortices shed from the bottom shear layer as these turbulent structures feature an opposite vorticity sign<sup>3</sup>.

Nonetheless, the Reynolds number governs the flow features developed around both ver-



26 tically and horizontally oriented cylinders. Several laboratory experiments and numerical  
 27 simulations focusing on the sub-critical flow regime ( $3 \cdot 10^2 < \text{Re} < 1 \cdot 10^5$ ) have highlighted  
 28 the higher shedding frequency of the shear layer generated vortices ( $f_{SL}$ ) compared to that  
 29 of the large-scale von-Kármán-type (VK) vortices ( $f_K$ ), where the frequency of the former  
 30 vortices can occur at a factor of 6.7 to 8.0 times greater than the wake ones<sup>4-7</sup>, and<sup>8</sup> demon-  
 31 strated the correlation between the ratio  $f_{SL}/f_K$  and Reynolds number. Furthermore, at  
 32 Reynolds number around 1,200 the shear layers separating from the cylinder's sides become  
 33 unstable undergoing laminar-to-turbulent transition due to Kelvin-Helmholtz instability<sup>8</sup>.  
 34 A transition in the sub-critical wake dynamics occurs at a Reynolds number around 5,000  
 35 to 5,500 where a distinct change in the shedding typology has been observed in both ex-  
 36 perimental and numerical studies<sup>7-9</sup>. This transition is distinguished by the presence of  
 37 undulations in the vortex filaments shedding across the cylinder span and the occurrence of  
 38 vortex dislocations<sup>7,9</sup> which also leads to a change from parallel to oblique vortex shedding<sup>8</sup>.  
 39 With increasing Reynolds number greater than 5,000 the wake typology remains unchanged  
 40 up to a Reynolds number of  $2 \cdot 10^5$ , which marks the beginning of the supercritical flow regime  
 41 where a significant change in the flow separation reduces the drag coefficient from values  
 42 ranging from 1.0–1.4 to between 0.2–0.4<sup>10-12</sup>. A detailed summary of the wake dynamics  
 43 dependency on Reynolds number is given in Williamson<sup>13</sup> and Sumner<sup>14</sup>.

44 A cylindrical body is often in close proximity of a solid boundary, for example, a pipeline  
 45 across an erodible river or sea bed, a bridge-pier close to an abutment or a mast located close  
 46 to a building. Only a few studies have examined the close proximity of a solid boundary  
 47 on a horizontal cylinder wake's flow structure<sup>1-3,15-19</sup>. In this configuration, the ratio of  
 48 the horizontal cylinder diameter ( $D$ ) and the vertical gap between the bottom wall and  
 49 the cylinder ( $G$ ), referred to hereafter as the gap ratio ( $G/D$ ), is highly influential on the  
 50 vortex dynamics developed downstream. For small gap ratios, e.g.  $G/D \leq 0.5$ , the wake  
 51 is asymmetric as a result of the difference in acceleration of the flow over and under the  
 52 cylinder, and the interaction of the under flow with the wall boundary layer. As the gap  
 53 ratio decreases the ground-effect increases, which causes the separation point on the upper  
 54 cylinder wall to move upstream while the separation point on the lower cylinder wall moves  
 55 downstream<sup>3</sup>. Furthermore, the frontal stagnation point moves towards the bottom wall and  
 56 an upwards force which increases with decreasing gap ratio is generated on the cylinder<sup>1,20,21</sup>  
 57 while the lower vortex is drawn upwards in the vertical direction immediately behind the

58 cylinder<sup>2,3</sup>. This leads to a separation bubble forming close to the bottom bed immediately  
 59 downstream of the wake bubble, which rapidly reduces in vertical and longitudinal extent  
 60 with increasing gap ratio<sup>3</sup>. At smaller gap ratios ( $G/D = 0.25$ ) and relatively low Reynolds  
 61 numbers, a bubble can also be formed at the wall immediately upstream of the cylinder  
 62 which rapidly reduces in extent with increasing  $G/D$  ratio<sup>3</sup>. As the gap ratio approaches  
 63 unity, the ground-effect vanishes causing the flow separation sequence and the recirculation  
 64 bubble to become more symmetric, i.e. the upper and lower laminar shear layers becoming  
 65 unstable at a similar distances downstream<sup>2,3</sup>.

66 The proximity of the wall alters the hydrodynamic forces on the horizontal cylinder  
 67 and the von-Kármán-type vortex shedding frequency depends on both the thickness of the  
 68 boundary layer and the gap ratio<sup>22,23</sup>. The upwards force on the cylinder is accompanied by a  
 69 reduction in the drag coefficient which decreases with decreasing gap ratio<sup>21</sup>. The proximity  
 70 of the wall also alters the dominant vortex shedding frequency, resulting in complex vortex-  
 71 boundary interactions. At lower Reynolds numbers ( $1.2 \cdot 10^3 < \text{Re} < 1.44 \cdot 10^3$ ) and gap  
 72 ratios ( $G/D < 0.5$ ), two distinct peaks observed in the power spectra of the root-mean-  
 73 square streamwise velocity have been attributed to the difference in motion between the  
 74 upper and lower vortices shed from the upper and lower cylinder sides respectively, resulting  
 75 in vortex-boundary interactions different from the unbounded cylinder condition<sup>3,16</sup>. Indeed,  
 76 for smaller gap ratios, the rms of the fluctuating lift coefficient is significantly lower for higher  
 77  $G/D$  ratios as a consequence of the suppression of the VK vortex shedding at the smaller  
 78  $G/D$  ratios<sup>3</sup>. The higher values of Strouhal number reported in these studies than those  
 79 from unbounded cylinder flow are therefore a result of the different development of the  
 80 vortex shedding and shear layers instability. With increasing gap ratio, the two peaks in the  
 81 shedding frequency merge into one single dominant peak<sup>3</sup> and periodic symmetric vortex  
 82 shedding occurs. Hence, at a critical gap ratio in the range of  $0.5 \leq G/D \leq 1.0$ , the Strouhal  
 83 number becomes independent of the gap ratio, approaching a value of around 0.2 commonly  
 84 found in cylinder flows unaffected by boundary effects<sup>3,16,21,24,25</sup>.

85 Additionally, at higher Reynolds numbers ( $4 \cdot 10^4 < \text{Re} < 1 \cdot 10^5$ ) a small gap ratio can not  
 86 only suppress VK vortex shedding but completely stop it<sup>1</sup>. For a cylinder with aspect ratio  
 87 ( $L/D$ ) of 8.33, the VK vortex shedding becomes intermittent at a gap ratio of 0.4 before  
 88 completely ceasing at a gap ratio of 0.3. At this lower gap ratio, a larger recirculation zone  
 89 is bounded by two nearly parallel shear layers from the cylinder sides, with no VK vortices

90 observed and only small-scale vortices generated from shear layers. The change in wake  
91 dynamics at a gap ratio of 0.3 is reflected in the drag coefficient reduction, which reaches a  
92 minimum at this gap ratio, and remains constant with decreasing  $G/D$  ratio<sup>1</sup>.

93 Irrespective of the experimental measurement technique and numerical model, it is com-  
94 monly agreed that the accurate measurement and prediction of the time-averaged high-order  
95 flow statistics in the near wake is highly challenging<sup>6,14,26</sup>. It has been postulated that there  
96 are different modes of low-frequency meandering of the near wake that may be responsi-  
97 ble for the large scattering of flow statistics<sup>6</sup>, which need to be resolved together with the  
98 high-frequency turbulence in the flow. Therefore, emphasis has been placed on the need  
99 to perform direct numerical simulations (DNS) or large-eddy simulations (LES) capable of  
100 resolving these flow characteristics conducted over a large number of shedding cycles in order  
101 to capture all the high- and low-frequency periodic motions. Numerical studies using LES  
102 and DNS have identified the wake's three-dimensionality by using different spanwise-length  
103 domains to capture the wavelength of the vortical structures across the cylinder span. For  
104 Reynolds numbers lower than 5,000, a minimum spanwise length of  $2\pi D$  is required to ac-  
105 curately capture even the longest wavelengths developed in the wake, which can influence  
106 the dynamic forces on the cylinder<sup>7</sup>, whereas a spanwise length of  $\pi D$  would only capture  
107 the turbulence structures in the shear layer and near-wake regions<sup>6,27,28</sup>.

108 There are few experimental and numerical test cases that have investigated a horizon-  
109 tal cylinder wake in the close proximity of a bottom wall boundary at moderate Reynolds  
110 numbers. The present study combines an experimental study with high-fidelity Large-Eddy  
111 Simulations (LES) in order to further elucidate the three-dimensional near wake flow struc-  
112 ture of a horizontal cylinder with wall proximity effects. The LES were conducted for gap  
113 ratios ( $G/D$ ) of 0.5 and 1.0 and for Reynolds numbers ( $Re$ ) equal to 6,666, 10,000 and 13,333  
114 while the experimental tests were conducted for the smaller gap ratio ( $G/D = 0.5$ ). To the  
115 best of our knowledge, these specific gap ratios have not been investigated for Reynolds  
116 numbers higher than the threshold  $Re = 5,000$  at which there is a distinct shift in the  
117 vortex shedding dynamics found in cylinder flows unaffected by boundary effects.

## II. EXPERIMENTAL SET-UP AND DATA PROCESSING

The experiments were conducted in a recirculating flume with glass sidewalls in the hydraulics laboratory at Cardiff University, United Kingdom. The flume had a rectangular cross-section, and was 10 m long, 0.3 m wide and 0.3 m deep. A horizontal cylinder of diameter ( $D$ ) 0.05m and length 0.3m was fixed 3.85 m downstream from the upstream inlet. The vertical gap ( $G$ ) between the flume bottom wall and the cylinder wall was 0.025 m giving a  $G/D$  ratio of 0.5. The flow structure in the cylinder wake was examined for three different flow discharges ( $Q$ ) of 6, 9 and 12  $ls^{-1}$ , which equated to cross-sectional bulk velocities of  $U_0 = 0.1333, 0.20$  and  $0.2667 \text{ ms}^{-1}$  respectively. The mean flow depth ( $H$ ) along the flume centreline remained fixed at 0.15 m for each flow condition and this was achieved by adjusting the downstream tailgate weir. The bed slope of the flume remained fixed at 1:1000. Table I presents details of the Reynolds numbers based on the cylinder diameter ( $Re = U_0 D / \nu$ ), bulk Reynolds number ( $Re_R = U_0 R / \nu$ , where  $R = A/P$  is the hydraulic radius,  $A$  is the cross-section area and  $P$  is the wetted perimeter) and Froude number ( $Fr = U_0 (gH)^{-0.5}$ , where  $g$  is the gravity acceleration) for the different flow conditions studied.

TABLE I: Details of the flow conditions studied: flow discharge ( $Q$ ), Reynolds number based on cylinder diameter ( $Re$ ), bulk Reynolds number ( $Re_R$ ), bulk velocity ( $U_0$ ), Froude number ( $Fr$ ) and estimated friction velocity ( $u_*$ ).

$Q \text{ [} ls^{-1} \text{]}$	$Re$	$Re_R$	$U_0 \text{ [} ms^{-1} \text{]}$	$Fr$	$u_* \text{ [} ms^{-1} \text{]}$
6	6,666	10,000	0.1333	0.110	0.020
9	10,000	15,000	0.2000	0.165	0.027
12	13,333	20,000	0.2667	0.220	0.033

Velocity measurements were collected using a Nortek 10 MHz Vectrino Plus Acoustic Doppler Velocimeter (ADV) at a sampling rate of 200 Hz and 300 s sampling time. This time period of ADV measurements are equivalent to approx. 255 shedding cycles for  $Q = 6ls^{-1}$  and 483 events for  $Q = 12ls^{-1}$ , based on the frequencies shown later in Section IV F. The cylindrical sampling volume (6 mm diameter and 7 mm height) was located at 50 mm from the probe transmitter. Thresholds of sound-to-noise ratio (SNR) and correlation (COR)  $> 20$

141 dB and  $>70\%$ , respectively, were maintained by seeding the water with silicate powder (10  
142  $\mu\text{m}$  average diameter and  $1.1 \text{ kgm}^{-3}$  density) and used for filtering the velocity time series.  
143 Despiking of time series used the Phase-Space Thresholding (PST) method by Goring and  
144 Nikora<sup>29</sup> as well as a 12-Point polynomial (12PP)<sup>30</sup>. Furthermore, by examining the velocity  
145 variances, data points identified as weak spots, which are errors resulting from acoustic  
146 pulse-to-pulse interference<sup>31</sup> were removed from the dataset. A velocity measurement grid  
147 resolution of 0.005 m and 0.02 m was used in the vertical ( $z$ ) and streamwise ( $x$ ) directions  
148 respectively, in the cylinder wake. This spatial resolution of the experimental data allowed  
149 effective capture of the dynamics of the wake structure. The velocity structure in the wake  
150 was measured along the channel centreline over a downstream distance of 0.3 m, i.e.  $6D$ . In  
151 the following, the symbols  $\langle \cdot \rangle$  indicates time-averaging operation.

## 152 Approach Flow Conditions

153 At a longitudinal distance of three diameters ( $3D$ ) upstream of the cylinder, vertical  
154 velocity profiles ( $z$ -direction) were measured as well as the lateral velocity distribution ( $y$ -  
155 direction) at the mid-flow depth ( $0.5H$ ) to capture the upstream flow boundary conditions.  
156 Fig. 2 presents a comparison of the measured approach flow profiles for the three discharges.  
157 The friction velocity ( $u_*$ ) was obtained from the best-fit of the velocity measurements to a  
158 log-law (Fig. 2b) that were measured for five flow conditions which included the three flow  
159 conditions modelled in this paper (i.e.  $Re = 6,666$ ,  $10,000$  and  $13,333$ ). Fig. 2a shows that  
160 the friction velocity increased linearly with the bulk velocity and thus the velocity profile  
161 approaching the cylinder can be defined according to a log-law distribution as,

$$\frac{u(z)}{u_*} = \frac{1}{\kappa} \ln \left( \frac{zu_*}{\nu} \right) \quad , \text{ where } u_* = 0.1036 \cdot U_0 + 0.00568 \quad (1)$$

162 Here  $\kappa$  is the von-Kármán constant equal to 0.41,  $z$  is the vertical coordinate considered  
163 and  $\nu$  is the kinematic viscosity. Levels of streamwise velocity fluctuations were similar for  
164 all discharges, being largest close to the flume's bed and decreased with increasing elevation  
165 (Fig. 2c). The depth-averaged turbulence intensity,  $\langle u' \rangle / U_0$ , was found to be around 10%  
166 for all cases. Fig. 2d shows that values of the cross-correlation of streamwise and vertical  
167 velocity fluctuations were largest for the lowest Reynolds number ( $Re = 6,666$ ) while similar

168 magnitudes were found for the  $Re = 10,000$  and  $13,333$ . Velocities measurements in the  
 169 transverse direction showed a negligible variation in streamwise velocities, therefore the flow  
 170 was assumed uniform across the flume width.

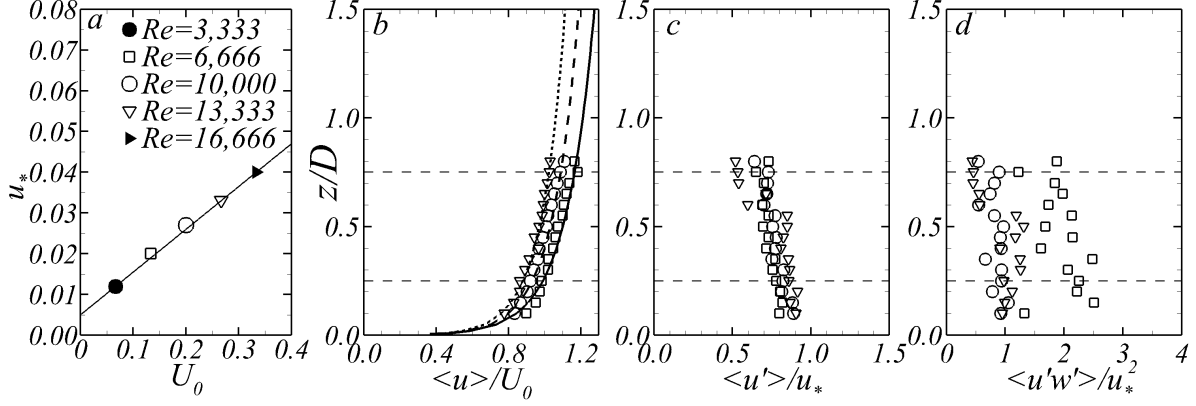


FIG. 2: Approaching inflow experimentally measured at a distance of  $3D$  upstream of the cylinder where (a) plots the bulk velocity ( $U_0$ ) against shear velocity ( $u_*$ ) derived from the velocity logarithmic profile fit (Eq. 1) for five flow conditions ranging from  $3,333 < Re < 16,666$ ; and vertical profiles of: (b) time-averaged streamwise velocity normalised by the bulk velocity, (c) streamwise velocity fluctuation normalised by shear velocity, and (d) vertical Reynolds shear stress normalised by the shear velocity squared for the three Reynolds number modelled in this study.

### 171 III. COMPUTATIONAL METHOD AND SET-UP

#### 172 A. Numerical framework

173 Eddy-resolving simulations are accomplished using the in-house code Hydro3D which  
 174 has been well-validated in hydro-environmental flows<sup>32–37</sup>. Hydro3D adopts the Large-Eddy  
 175 Simulation (LES) approach to explicitly resolve the energy-containing flow structures while  
 176 modelling the scales smaller than the grid size using a sub-grid scale model. The governing  
 177 equations are the spatially filtered Navier-Stokes equations for incompressible, viscous flow  
 178 that are solved in a Eulerian coordinate system, and are as follows:



$$\frac{\partial u_i}{\partial x_i} = 0 \quad (2)$$

$$\frac{\partial u_i}{\partial t} + \frac{\partial u_i u_j}{\partial x_j} = -\frac{\partial p}{\partial x_i} + \nu \frac{\partial^2 u_i}{\partial x_j \partial x_j} - \frac{\partial \tau_{ij}}{\partial x_j} + f_i \quad (3)$$

Here,  $u_i = (u, v, w)$  and  $x_i = (x, y, z)$  are the filtered fluid velocity and position in the three coordinates of space respectively,  $p$  denotes filtered pressure,  $\nu$  is the fluid kinematic viscosity,  $\rho$  is the fluid density, and  $\tau_{ij}$  is the sub-grid scale stresses. The sub-grid scale stress tensor is approximated using the WALE subgrid scale model<sup>38</sup> considering a filter size equal to the grid size. The forcing term  $f_i$  represents external forces calculated using the direct forcing Immersed Boundary method<sup>39</sup>, here used to represent the cylinder geometry<sup>40</sup>.

In Hydro3D the fluxes are calculated using a pure second-order central differencing scheme with staggered storage of the velocity components on a rectangular Cartesian grid. The fractional-step method is used with a three-step Runge-Kutta predictor to approximate convective and diffusive terms, and an efficient multi-grid technique is adopted to solve a Poisson pressure-correction equation as a corrector at the final step. Hydro3D uses the domain decomposition technique to divide the computational domain into rectangular sub-domains and is parallelised with Message Passing Interface (MPI)<sup>41</sup>. It also features a local mesh refinement method<sup>42</sup> that permits a higher spatial grid resolution near the cylinder and a coarser grid resolution with increasing distance away from the cylinder, thus reducing the computational expense.

## B. Computational setup

The schematic of the computational domain presented in Fig. 3 comprises  $30D$  in the streamwise direction,  $6D$  in the cross-streamwise direction and  $3D$  in the vertical direction, therefore replicating the full flume width and the uniform flow depth used in the experiments. Note the spanwise domain length ( $6D$ ) is very close to the proposed length of  $2\pi D$  required to fully capture the spanwise wavelength of the vortical structures in the cylinder wake<sup>7</sup>. The downstream end of the cylinder is located  $7D$  from the upstream inlet and considered as the origin of the  $x$ -coordinates. Two cylinder locations were studied with LES, one adopting the gap ratio as studied in the experimental study and another case with a gap ratio of 1.0,

which is indicative of the case where the cylinder is unaffected by proximity to the bottom wall.

The same grid resolution is adopted for the two lower Reynolds numbers ( $Re = 6,666$  and  $10,000$ ) whilst the resolution is doubled for the highest Reynolds number case ( $Re = 13,333$ ) due to an increase in the friction velocity and the requirement to keep the first grid cell off the wall within the viscous sub-layer<sup>43</sup>. The grid resolution adopted is the same in  $x$ - and  $z$ -directions ( $\Delta x = \Delta z$ ), whilst it was doubled in the spanwise direction, i.e.  $\Delta y = 2\Delta z$ . The resolution in the computational domain is non uniform in the streamwise direction, as local mesh refinement is adopted<sup>42</sup>, but uniform in the spanwise and vertical extensions. A fine grid size is adopted in the region embedding the cylinder and the near-wake between  $x = -1D$  and  $5D$ , whilst the grid size is doubled in the remaining domain to reduce the computational burden of the simulations. Table II details the mesh resolution in the fine grid region ( $\Delta z$ ) for three flow conditions examined, grid resolution of the first cell off the wall in wall-units ( $\Delta z^+$ ) and millions of fluid cells comprising the entire computational domain. In the far-wake after  $x/D > 20$ , the resolution in wall units of  $\Delta y^+$  and  $\Delta z^+$  reach values up to 2 and 18, respectively.

TABLE II: Specification of the computational grid resolution used and total number of fluid cells for each of the cases analysed.

$Re$	$U_0 [ms^{-1}]$	$\Delta z [m]$	$\Delta z^+$	Grid cells
6,666	0.1333	$6.250 \times 10^{-4}$	6.25	$14.32 \times 10^6$
10,000	0.2000	$6.250 \times 10^{-4}$	8.44	$14.32 \times 10^6$
13,333	0.2666	$3.125 \times 10^{-4}$	5.16	$82.94 \times 10^6$

The log-law velocity profile (Eq. 1) is prescribed at the inlet of the domain and adjusted for each of the examined flow discharges. A convective condition is used at the outlet and no-slip conditions were imposed at the bottom and lateral walls, which is justified from the values of  $\Delta z^+$  indicating that the first point off the wall is within the viscous sub-layer. A shear-free rigid-lid condition<sup>44</sup> is employed to represent the water surface as the influence of free-surface effects is considered small when the maximum  $Fr$  is relatively low (0.22), and this is defined as,

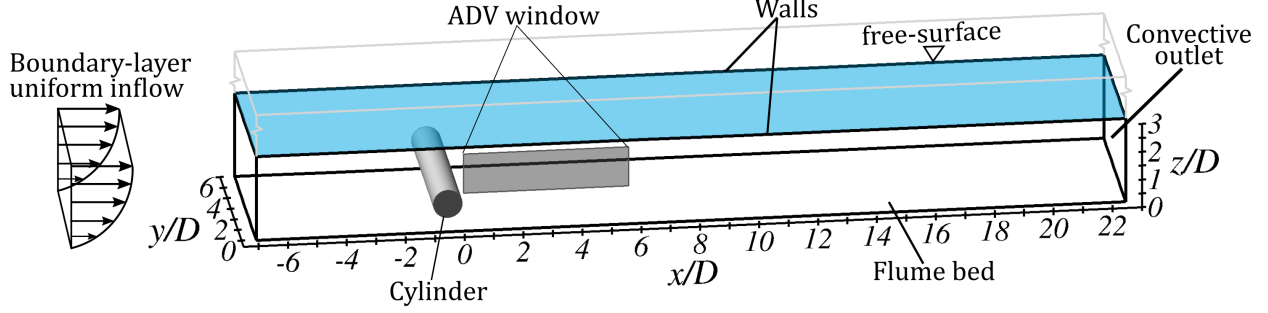


FIG. 3: Schematic of the computational domain with the imposed boundary conditions showing location of horizontal cylinder and laboratory ADV measurement control volume.

$$\frac{\partial u}{\partial z} = 0 \quad ; \quad \frac{\partial v}{\partial z} = 0 \quad ; \quad w = 0 \quad \text{for } z = H \quad (4)$$

The simulations are initially run until flow transients have vanished. First order statistics are then collected for a total simulation time in terms of non-dimensional time  $t^* = tD/U_0$  of 260 equating to 32 eddy turn-over time ( $t_e = H/u_*$ ). Second-order statistics are collected after  $t^* = 60$  for a total of  $200D/U_0$  representing approximately 170 shedding cycles. A Courant-Friedrichs-Lewy (CFL) condition of 0.7 is set to ensure numerical stability. The computations are performed on 170 Intel Skylake Gold 6148 @2.40GHz cores using Supercomputing Wales facilities with a total computational load of 225,000 CPU hours for the highest Reynolds number case ( $Re = 13,333$ ).

## IV. RESULTS AND DISCUSSION

### A. Time-averaged nature of the flow

Results of the time-averaged flow developed around the cylinder for the  $G/D$  and  $Re = 6,666$  case are shown in Fig. 4 along the channel centreline plane, i.e.  $y/D = 3$ . The distribution of streamwise velocities evidences how the approaching flow impinges the cylinder and accelerates over and beneath it, as depicted from Fig. 4a. Flow streamlines indicate that the recirculation area immediately behind the cylinder is mostly symmetric and extends until approximately  $1D$  downstream. After  $x/D = 1$ , the streamwise velocities significantly diminish outside of the wake bubble on the lower side of the wake, i.e.  $z/D < 0.5$ , compared to the high-momentum region located above the wake ( $z/D = 1.5$ ). Fig. 4b presents the

contours of time-averaged vertical velocities showing the asymmetry in the flow influenced upstream by the logarithmic distribution of the approaching flow and downstream by the closer proximity of the cylinder to the channel bottom than free-surface layer. The area of high vertical velocities in the lower part of the near-wake is a result of the bed-effect as the fluid accelerates through the vertical gap between the cylinder and flume bed.

The lack of a more pronounced asymmetry in the recirculation bubble despite the small gap ratio  $G/D$  of 0.5 is somewhat expected as this  $G/D$  ratio corresponds to the intermediate range in which the influence of the ground-effect in the time-averaged flow field is deemed small<sup>1,2</sup>. This can be observed from the streamlines in Fig. 4a which show the lower half of the wake extending over the wake centreline, i.e.  $z/D > 1$ , until a distance  $x/D = 5$ , whilst in the upper layer near the free-surface layer the streamlines are nearly parallel. This asymmetric flow pattern is further indicated by the distribution of the vertical velocities whose magnitude becomes notably reduced after  $x/D = 1.5$ . It is worth noting that no wall boundary layer separation upstream of the cylinder occurs, as the Reynolds numbers of the present flow conditions are well above the threshold of  $Re = 1,400$  at which such separation vanishes<sup>16</sup>.

The examined cases are for Reynolds numbers within the sub-critical cylinder flow regime in which the shear layers are laminar whilst the wake is fully turbulent, i.e. the present unsteady wake lies within the shear-layer transition regime identified in Williamson<sup>13</sup>, in which shear layers remain laminar immediately after departing from the cylinder's sides. As shown later in Section IV E, these start to become unsteady at a closer distance to the cylinder with increasing  $Re$ , due to Kelvin-Helmholtz instability. This laminar-to-turbulence transition of the turbulent structures is accompanied by the turbulent nature of the near-wake enclosed to the downstream side of the cylinder. Levels of computed streamwise turbulence intensity (Fig. 4c) are larger than  $\langle u' \rangle / U_0 = 0.6$  indicating that the near-wake is remarkably unsteady. There is also an uneven distribution of  $\langle u' \rangle$  along the centreline of the cylinder wake ( $z/D = 1$ ) with the turbulent region below this elevation extending almost twice the length than in the region higher up in the wake. Interaction between the cylinder-induced near-wake and the ground can be appreciated from the distribution of high  $\langle u' \rangle$  values near the bed between  $0 < x/D < 2$  reaching values up to 0.65.

The asymmetry of the turbulent wake in the downstream direction is again depicted in the distribution of  $\langle w' \rangle$  presented in Fig. 4d with a well-defined area of  $\langle w' \rangle / U_0 > 0.7$  found

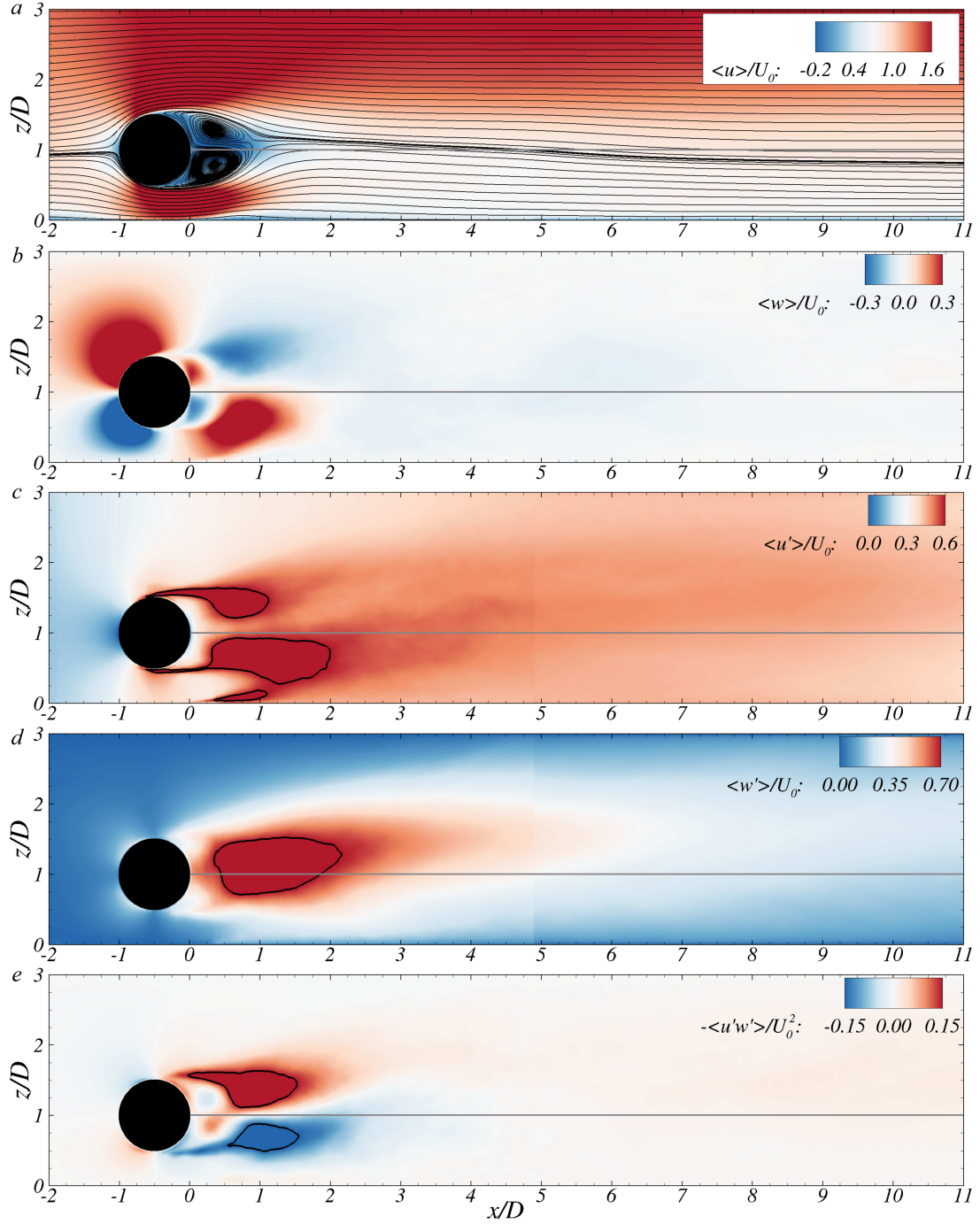


FIG. 4: Side elevation contour plots of the LES computed (a) streamwise velocity, (b) vertical velocity, (c) streamwise turbulence intensity with lines denoting  $\langle u' \rangle / U_0 = 0.6$ , (d) vertical turbulence intensity with lines denoting  $\langle w' \rangle / U_0 = 0.7$ , and (e) Reynolds shear stress with the solid lines corresponding to  $\langle u'w' \rangle / U_0^2 = \pm 0.15$ , normalised by the bulk velocity for the  $Re = 6,666$  and  $G/D = 0.5$  case.

278 between  $0.4 < x/D < 2.2$ . Interestingly a larger portion of this high vertical turbulence  
 279 intensity region is located above the cylinder centreline,  $z/D = 1$ , whilst predominantly  
 280 below the centreline for the streamwise turbulence intensity (Fig. 4c). This evidences  
 281 that the ground-effect renders the nature of the near-wake significantly more unsteady by  
 282 changing the dynamics of the vortex generation and shedding which, in consequence, leads  
 283 to an asymmetric wake distribution. A similar pattern is found in the distribution of vertical  
 284 Reynolds shear stress ( $\langle u'w' \rangle$ ); where higher Reynolds shear stresses values above  $z/D =$   
 285 1 result from the higher momentum exchange between the flow overtopping the cylinder  
 286 with the near wake than that with the flow moving under the cylinder. Overall, the time-  
 287 averaged second-order statistics ( $\langle u' \rangle$ ,  $\langle w' \rangle$ ,  $\langle u'w' \rangle$ ) indicate that until  $x/D = 2$  the wake is  
 288 very turbulent, followed by a region between  $2 < x/D < 5$  over which turbulence decays  
 289 and is distributed uniformly over the water depth, as the wake expands over the entire  
 290 water column. Moreover, negligible differences in these time-averaged flow statistics with  
 291 increasing Reynolds number are observed, as shown in Fig. 20 for the  $G/D = 0.5$  and  $Re$   
 292  $= 13,333$  case.

293 The main hydrodynamics developed for the case with gap ratio  $G/D$  equal to 1.0 for  $Re$   
 294  $= 6,666$  are presented in Fig. 5. Increasing the distance from the cylinder to the ground  
 295 leads to the recovery of the wake symmetry, as seen in the distribution of the main velocity  
 296 components  $\langle u \rangle$  and  $\langle w \rangle$ . Contours of  $\langle u' \rangle$ , which represent the streamwise fluctuations  
 297 derived from the shear layers and near wake dynamics, are again symmetric and notably  
 298 different from their distribution in the  $G/D = 0.5$  case (Fig. 4c). A small deviation from  
 299 the centreline is observed in the  $\langle w' \rangle$  contours at  $x/D = 3$ , these fluctuations being larger in  
 300 the upper part of the wake owed to the logarithmic inflow velocity distribution. Similarly,  
 301 the two regions of Reynolds shear stress  $\langle u'w' \rangle$  attached to the cylinder's downstream face  
 302 have different length, which indicate that even with  $G/D = 1.0$  the wake is not precisely as  
 303 that in unbounded cylinder flows.

304 Fig. 6 presents the vertical profiles of  $\langle u \rangle$  and  $\langle u' \rangle$  at nine locations downstream of the  
 305 cylinder obtained from the experiments and the LES for the cases of  $Re = 10,000$  and 13,333  
 306 and  $G/D = 0.5$ . At the locations closest to the cylinder, i.e.  $x/D < 1.2$ , there is a significant  
 307 velocity deficit behind the cylinder. LES captures well the distribution of  $\langle u \rangle$  and  $\langle u' \rangle$  over  
 308 the water depth. The slight vertical offset of the computed wake is attributed to the fact  
 309 LES treats the free-surface as a shear-free rigid lid whilst water surface waviness was present



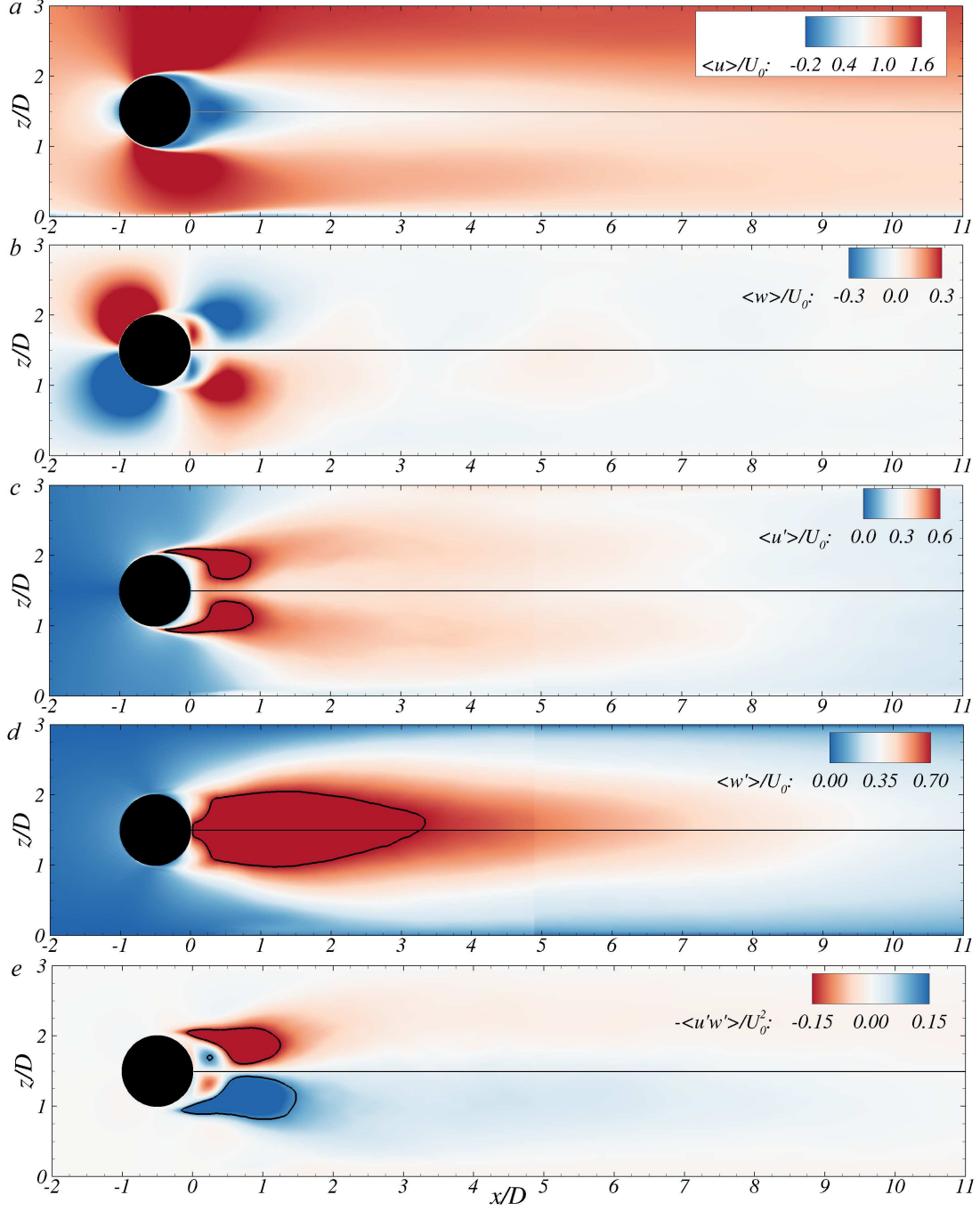


FIG. 5: Side elevation contour plots of the computed (a) streamwise velocity, (b) vertical velocity, (c) streamwise turbulence intensity with lines denoting  $\langle u' \rangle / U_0 = 0.6$ , (d) vertical turbulence intensity with lines denoting  $\langle w' \rangle / U_0 = 0.7$ , and (e) Reynolds shear stress with the solid lines corresponding to  $\langle u'w' \rangle / U_0^2 = \pm 0.15$ , normalised by the bulk velocity for the  $Re = 6,666$  case and  $G/D = 1.0$ .

310 in the experiments, particularly immediately after the cylinder. Further downstream, the

streamwise velocity tends to recover and approach the unperturbed log-law profile found upstream of the cylinder. Until a distance of  $x/D \approx 3$ , the profiles of  $\langle u' \rangle$  feature one peak over the cylinder top (i.e.  $z/D > 1.5$ ) and another that is larger in magnitude at  $z/D \approx 0.5$ . Such asymmetrical distribution of  $\langle u' \rangle$  evidences the ground-effect in the von-Kármán street as also observed in Fig. 4c. A more uniform distribution along the water column is found after  $x/D = 3$  indicating that the shed vortices have merged as explained later in Section IV C.

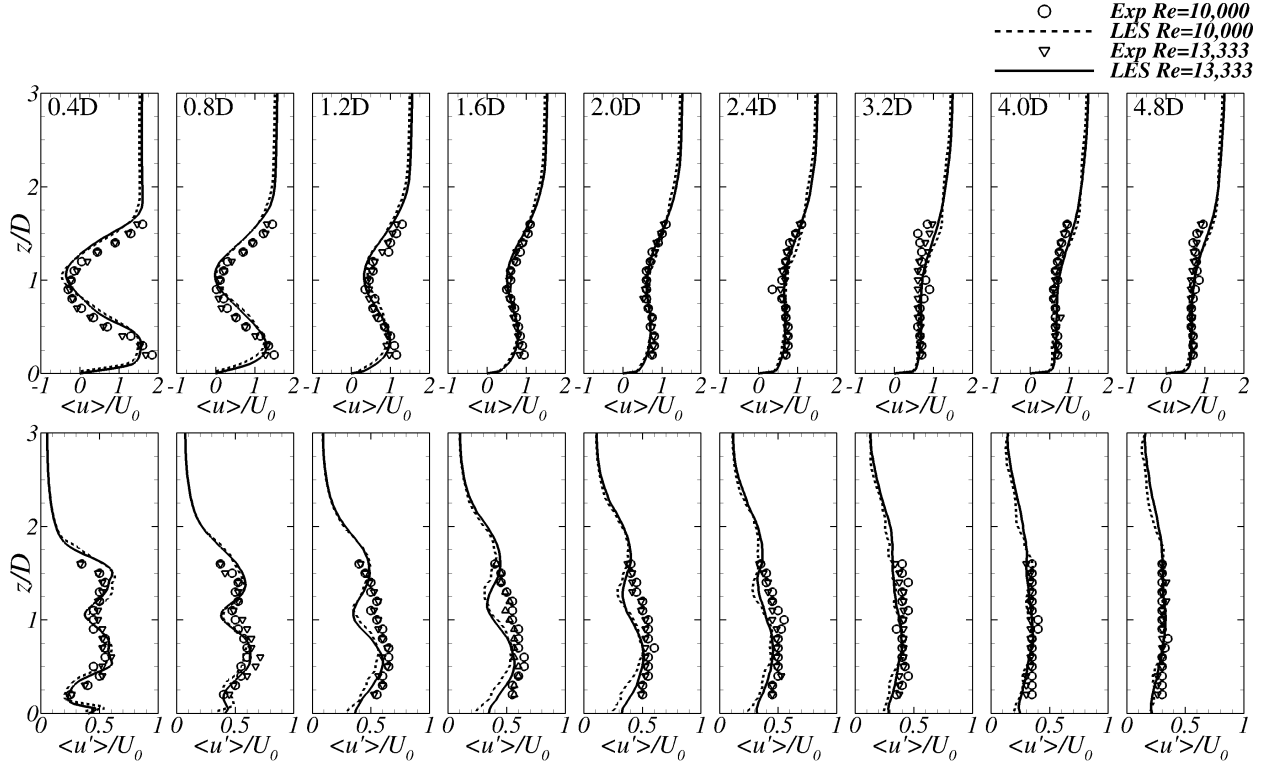


FIG. 6: Vertical profiles of mean streamwise velocity  $\langle u \rangle$  (top) and turbulence intensity  $\langle u' \rangle$  (bottom) at different locations downstream of the cylinder for the  $Re = 10,000$  and  $13,333$  cases and  $G/D = 0.5$ . Comparison between experimental (symbols) and LES (lines) results.

The vertical distribution of mean vertical velocity  $\langle w \rangle$  and turbulence intensity  $\langle w' \rangle$  from the experiments and LES at the channel centreplane, i.e.  $y/D = 0.0$ , is shown in Fig. 7 for the  $Re = 10,000$  and  $13,333$  cases and  $G/D = 0.5$ . Profiles immediately behind the cylinder show a marked upwards fluid motion below the cylinder centreline resulting from the flow acceleration through the bed-cylinder gap. Vertical turbulence intensity profiles show that near the bluff body the maxima are attained along the cylinder centreline however further

324 downstream the peak of  $\langle w' \rangle$  shifts towards the free-surface as a result of the von-Kármán  
 325 vortices moving to the region of highest momentum. LES overpredicts the values of  $\langle w \rangle$   
 326 close to the bed immediately behind the cylinder while there is a good match with the  
 327 experimental results above the cylinder centreline ( $z/D = 1.0$ ). A similar pattern is found  
 328 for  $\langle w' \rangle$  in the near-wake, although LES achieves a good match with experimental results  
 329 immediately behind the wake bubble ( $x/D > 1.2$ ). Overall, the normalised distribution of  
 330 these mean quantities follows a very close distribution for the three cases, the remaining  
 331 sources of data disparity are probably related to not modelling the free-surface deformation  
 332 and the fact that inflow conditions used in the LES differed from the fully developed flow  
 333 attained in the experiments which can affect the near-wake results.

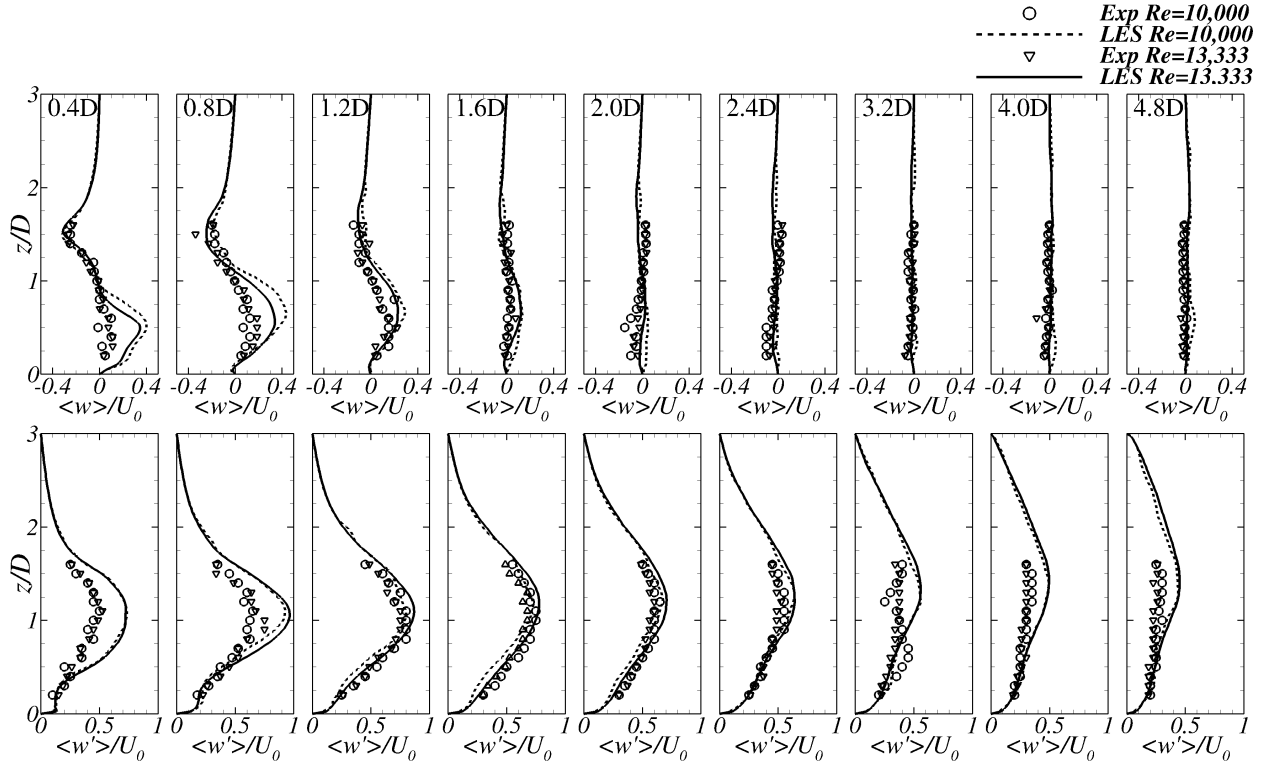


FIG. 7: Vertical profiles of mean vertical velocity  $\langle w \rangle$  (top) and turbulence intensity  $\langle w' \rangle$  (bottom) at different locations downstream of the cylinder for the  $Re = 10,000$  and  $13,333$  cases and  $G/D = 0.5$ . Comparison between experimental (symbols) and LES (lines) results.

## 334 B. Recirculation region

335 Further insights into the asymmetric wake enclosed behind the cylinder for the different  
 336 flow rates studied with  $G/D = 0.5$  are given in Fig. 8. The flow streamlines indicate that  
 337 in all cases the two recirculating cells are not symmetrically distributed about the cylinder  
 338 centreline and are slightly shifted towards the free-surface. This shift is more pronounced  
 339 with increasing Reynolds number. The spatial resolution of the flow streamlines used to  
 340 deduce the separation point off the cylinder sides is approximately half of the grid size.  
 341 The recirculation length ( $L_{rec}/D$ ) shortens with increasing Reynolds number as presented  
 342 in Table III, and its values are similar to those reported for unconfined cylinder flows<sup>6,7</sup>.  
 343 Results also show that increasing the gap ratio decreases the recirculation length due to the  
 344 change in the wake recovery dynamics<sup>26</sup>. Similarly, the streamwise location of the upper and  
 345 lower recirculation cores,  $x_{up}^c$  and  $x_{low}^c$ , is closer to the cylinder for larger Reynolds numbers,  
 346 whilst the vertical core location,  $z_{up}^c$  and  $z_{low}^c$ , increases as a result of a larger mean wake  
 347 asymmetry. For the  $G/D = 1.0$  case, the loci of both upper and lower recirculation cores  
 348 are symmetric to the wake centreline, the upper cell being slightly longer as shown in Table  
 349 III. Flow streamlines allow the precise location at which the boundary layers separate on  
 350 both upper and lower halves of the cylinder. Both separation points move upstream with  
 351 increasing Reynolds number, as shown in previous studies<sup>2</sup>, and coincide with the successive  
 352 reduction of the separation angles at the upper ( $\theta^{up}$ ) and lower ( $\theta^{low}$ ) half of the cylinder,  
 353 as presented in Table III. From Fig. 8, it is also observed that the locus of the upper cell is  
 354 closer to the cylinder than the bottom cell as the fluid flows faster under the cylinder than  
 355 over it, which is again reflected in values of  $\theta^{low}$  being larger than  $\theta^{up}$ . Interestingly, for the  
 356 three flow conditions studied, two laminar separation bubbles appear enclosed between the  
 357 lee-side of the cylinder and the recirculation cells.

358 Comparison of the impact of the proximity to the ground in the recirculation area behind  
 359 the cylinder is shown in Fig. 9. For the largest gap ratio, the streamlines distribution is  
 360 symmetric to the wake centreline whilst for  $G/D = 0.5$  the asymmetry is observed even at  
 361 distances larger than  $x/D = 4$  downstream. Another representation of the time-averaged  
 362 dynamics of the vortex shedding is the mean spanwise vorticity ( $\omega_y$ ) presented in Fig. 9b. In  
 363 both cylinder positions, two regions of high vorticity are developed in the shear-layer region,  
 364 and this is mostly symmetric for  $G/D = 1.0$ . For the case with the cylinder impacted by

TABLE III: Characteristics of the recirculation area for the different cases analysed: normalised recirculation length ( $L_{rec}/D$ ), location of the upper and lower recirculation cores ( $x^c, z^c$ ) and upper ( $\theta^{up}$ ) and lower ( $\theta^{low}$ ) separation angles.

Re	$G/D$	$L_{rec}/D$	$x_{up}^c$	$x_{low}^c$	$z_{up}^c$	$z_{low}^c$	$\theta^{up}$ [deg]	$\theta^{low}$ [deg]
6,666	0.5	1.389	0.837	0.895	0.303	-0.218	95.7	101.3
6,666	1.0	1.118	0.760	0.747	0.252	-0.259	93.4	90.6
10,000	0.5	1.348	0.792	0.876	0.316	-0.200	92.9	97.6
10,000	1.0	1.117	0.728	0.737	0.252	-0.256	91.7	85.6
13,333	0.5	1.233	0.785	0.855	0.307	-0.198	86.6	95.7
13,333	1.0	1.066	0.741	0.697	0.246	-0.276	85.0	83.5

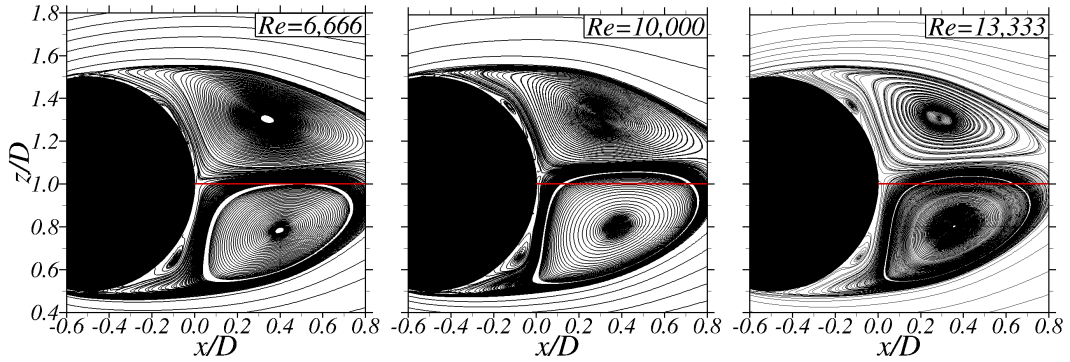


FIG. 8: Mean recirculation region computed using LES with  $G/D = 0.5$ . Red line indicates the cylinder centreline at  $z/D = 1.0$ . Flow is from left to right.

the ground effect, the upper region of high vorticity extends slightly longer than the bottom one which is influenced by the ground-vortex, as explained later in Section IV E.

### C. Centreline profiles

The distribution of the mean flow field along the cylinder centreline ( $z/D = 1$ ) with increasing downstream distance from the cylinder for  $G/D = 0.5$  is shown in Fig. 10 with longitudinal profiles of mean streamwise and vertical velocities, and turbulence intensities from both the experiments and LES. Fig. 10a shows the velocity reversal in the attached

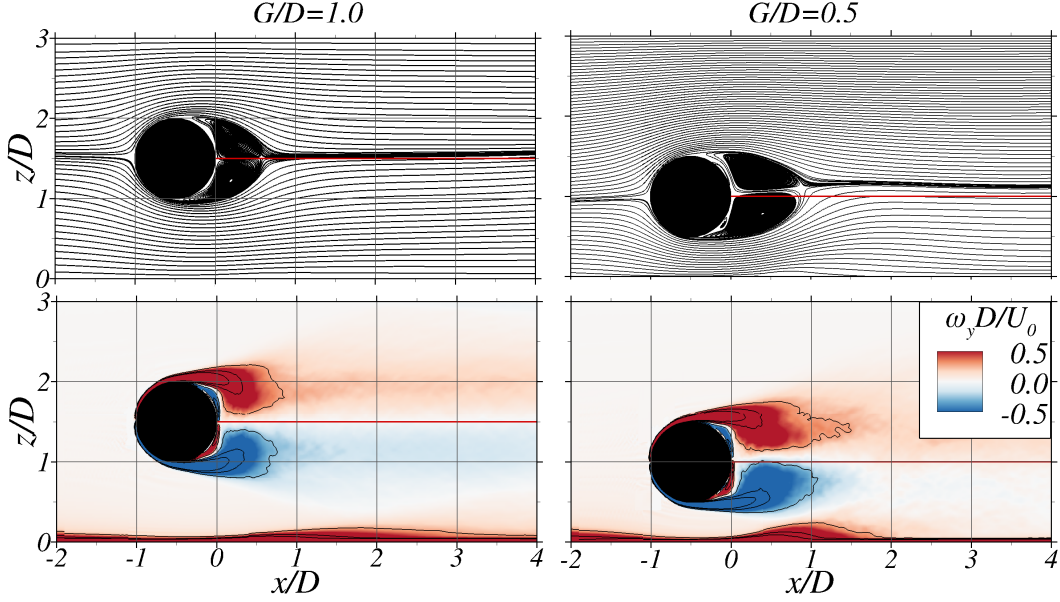


FIG. 9: Comparison of the mean recirculation region (top) and spanwise vorticity from the LES of the cylinder at  $G/D = 1.0$  (left) and  $0.5$  (right) for  $Re = 13,333$ . Red line indicates the cylinder centreline at  $z/D = 1.0$ . Flow is from left to right.

recirculation area with a peak reversal of  $-0.4U_0$ . The recirculation area ends by  $1D$  downstream of the cylinder as indicated by the positive streamwise velocity. For all cases analysed, the streamwise momentum has nearly recovered, i.e.  $\langle u \rangle / U_0 \approx 0.8$ , by a downstream distance of  $3D$ , and there is a good agreement between measured data and LES. Fig. 10b shows that there is a similar trend in the evolution of  $\langle u' \rangle$  for cases of  $Re = 6,666$  and  $10,000$ , with experiments and LES data almost coinciding to a value close to  $\langle u' \rangle = 0.4U_0$  at a downstream distance of  $3D$ , after which the streamwise turbulence intensities progressively decay with increasing downstream distance. However, in the near-wake the computed streamwise turbulence intensities are lower than the experiments, attributed to the lack of resolving the free-surface which may lead to a slight change in the vortex generation dynamics.

Centreline plots for  $\langle w \rangle$  from Fig. 10c show that in the region between  $1-2D$  immediately downstream of the wake bubble, i.e. where the large-scale vortices are shed, there is a peak in positive  $\langle w \rangle$  denoting predominant upwards fluid motion. The ground-effect is responsible for suppressing the symmetry in the vortex shedding mechanism compared to unbounded cylinder flows, which feature zero values of  $\langle w \rangle$  along the cylinder centreline. By a downstream distance of  $2D$ , the vertical velocities decrease and by  $10D$  these are essentially zero for all three flow conditions. Regarding the distribution of vertical turbulence intensity (Fig.



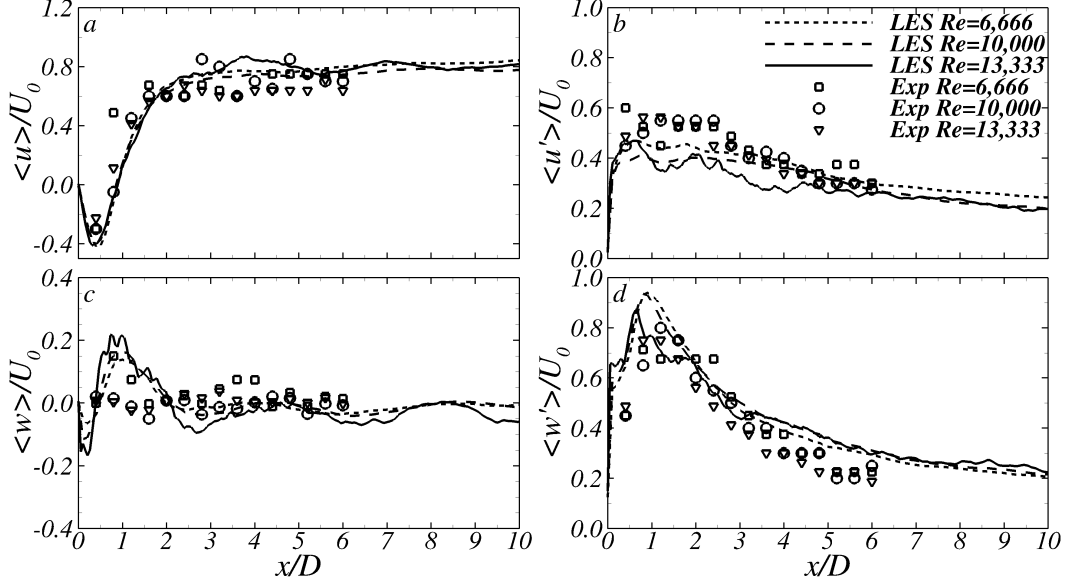


FIG. 10: Centreline profiles of normalised  $\langle u \rangle$ ,  $\langle u' \rangle$ ,  $\langle w \rangle$  and  $\langle w' \rangle$  from experiments and LES for the three Reynolds numbers and  $G/D = 0.5$ .

10d) the maxima are achieved at  $x/D = 1$  for the LES and at  $x/D = 1.5$  in the experiments, which are significantly larger than those found for the streamwise turbulence intensity. Close agreement between computed and measured results is observed by a downstream distance of  $2D$  with  $\langle w' \rangle$  attaining a value of nearly  $0.7U_0$  and progressively decaying until  $0.2U_0$  further downstream.

#### D. Continuity equation terms analysis

The asymmetric near-wake recovery can be further characterised by considering the mean velocity terms in the continuity equation:

$$\frac{\partial \langle u \rangle}{\partial x} + \frac{\partial \langle v \rangle}{\partial y} + \frac{\partial \langle w \rangle}{\partial z} = 0 \quad (5)$$

In an unbounded environment these terms should be symmetric to the cylinder centreline but are expected to change in the present case due to the proximity of the cylinder body to the flume bed. The term  $\partial \langle v \rangle / \partial y$  is deemed much smaller than the other two as the main flow direction is in the  $xz$ -plane. Fig. 11 presents the contour plots of the terms  $\partial \langle u \rangle / \partial x$  and  $\partial \langle w \rangle / \partial z$  for the  $Re = 13,333$  case for both gap-to-diameter ratios. For the short gap

402 case, the regions of highest rate-of-change of  $\langle u \rangle$  in the streamwise direction are found in the  
 403 core of the near-wake between  $0 < x/D < 2$  and  $0.5 < z/D < 1.5$ . For this configuration,  
 404 the streamwise change of  $\langle u \rangle$  is asymmetric to the wake centreline due to its proximity to  
 405 the ground, whilst with  $G/D = 1.0$  the term  $\partial\langle u \rangle/\partial x$  is symmetric to the centreline. In  
 406 both cases, these regions coincide with those with the largest negative rate-of-change of  
 407  $\partial\langle w \rangle/\partial z$ , as both terms need to balance in Eq. 5. A region of negative  $\partial\langle u \rangle/\partial x$  develops  
 408 over the upper shear layer until  $x/D \approx 0.5$  indicating a decrease in  $x$ -velocities along the  
 409 streamwise direction, irrespective of the cylinder position. However, with  $G/D = 0.5$ , in the  
 410 gap between the flume's bed and cylinder such a region of  $\partial\langle u \rangle/\partial x < 0$  extends until  $x/D <$   
 411 1.5 as a result of the wake dynamics affected by the close proximity to the ground.

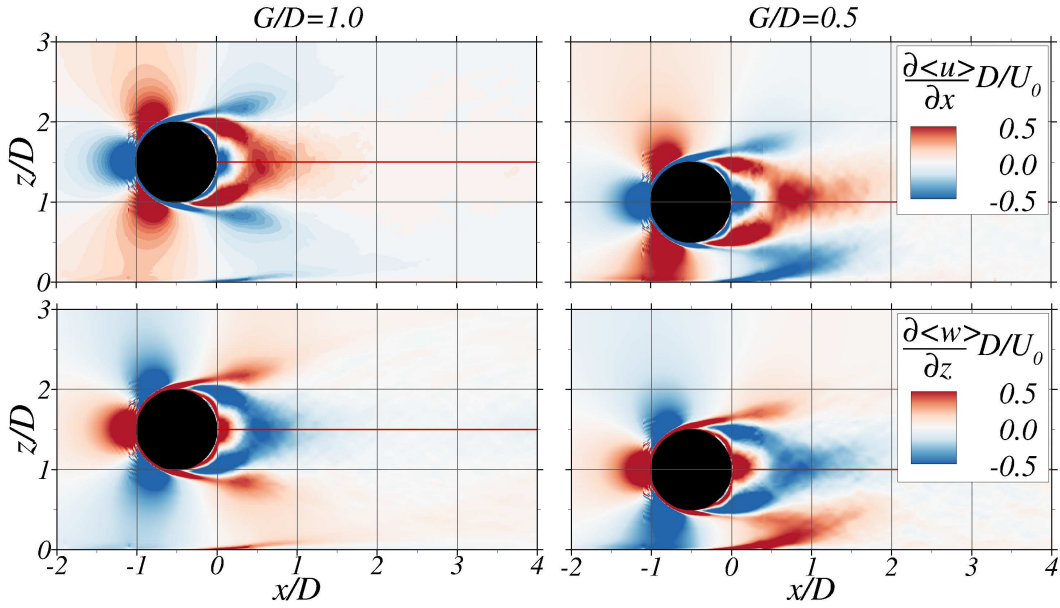


FIG. 11: Contours of the continuity equation terms for the  $Re = 13,333$  case with  $G/D =$   
 1.0 (left) and 0.5 (right).

412 Upstream of the cylinder, an area of  $\partial\langle u \rangle/\partial x > 0$  is present as the approach flow accel-  
 413 erates on its upper and lower sides, whilst a reduction of  $\langle u \rangle$  is seen near the stagnation  
 414 point. A reverse distribution is found for  $\partial\langle w \rangle/\partial z$  in the near-wake of the cylinder. Both  
 415 terms from the continuity equation show minor variations amongst the three flow discharges  
 416 analysed for both geometries analysed, with the mass conservation (Eq. 5) being satisfied.

## 417 E. Instantaneous flow structures

418 The unsteady nature of the flow structures developed behind the cylinder are shown in  
 419 Fig. 12 with contours of  $y$ -vorticity at three different spanwise locations ( $y/D = 0.5, 3.0$   
 420 and  $5.0$ ) for the case  $Re = 6,666$  with  $G/D = 0.5$ , which shows the spanwise variation of the  
 421 vortical structures. Shear layers are developed along the cylinder surface and separate on the  
 422 lee-side featuring a laminar nature until becoming unstable due to the shear caused by the  
 423 low-momentum near-wake and the fast-flowing fluid over the cylinder. Following a Kelvin-  
 424 Helmholtz instability, the shear layers breakdown into small vortices (or KH vortices) that  
 425 are convected downstream, eventually merging with the fully-turbulent near-wake between  $0$   
 426  $< x/D < 1$ . Such flow separation is expected at these Reynolds numbers as they correspond  
 427 to the sub-critical regime.

428 The transition from the shear layers to the generation of KH vortices is non uniformly  
 429 distributed across the entire spanwise length of the cylinder as observed from the spanwise-  
 430 vorticity contours. Such three-dimensional variation of the shear layers' roll-up is known as  
 431 intermittency that is a function of the spanwise distance<sup>45,46</sup>. The onset of KH instabilities  
 432 developed in the upper and lower shear layers are decorrelated, i.e. there is no synchronisation  
 433 in their generation, e.g. at  $y/D = 0.5$  the first roller developed from the lower shear is  
 434 observed at  $x/D \approx 0.2$  whilst the upper shear layer has rolled up shortly after its separation  
 435 point from the cylinder transitioning to turbulent flow. Here, only the Reynolds number  
 436  $6,666$  case is shown for brevity. Nonetheless, similar instantaneous flow patterns in the near-  
 437 wake are observed for all Reynolds numbers examined although there are some differences,  
 438 e.g. more rapid breakdown of the shear layers with a higher Reynolds number, as indicated  
 439 by the different separation angles show in Fig. 8 and the values presented in Table III.

440 In the region between  $1 < x/D < 2$ , the attached unstable near-wake transitions to  
 441 large-scale von-Kármán vortices, characteristic of the far-wake behind bluff bodies. Here the  
 442 proximity of the cylinder to the flume bed for the case  $G/D = 0.5$  leads to the generation of  
 443 a wall shear layer and a subsequent ground-vortex (GV) as depicted in Fig. 12. This region  
 444 of flow separation originates from the low-pressure generated by the unsteady wake during  
 445 the formation of the rollers off the lower shear layer of the cylinder. Three regions can be  
 446 distinguished: a stable shear layer until  $x/D = 1$ , a separation bubble and the eventual  
 447 generation of the GV. The latter eventually grows and dettaches, lifting off the ground

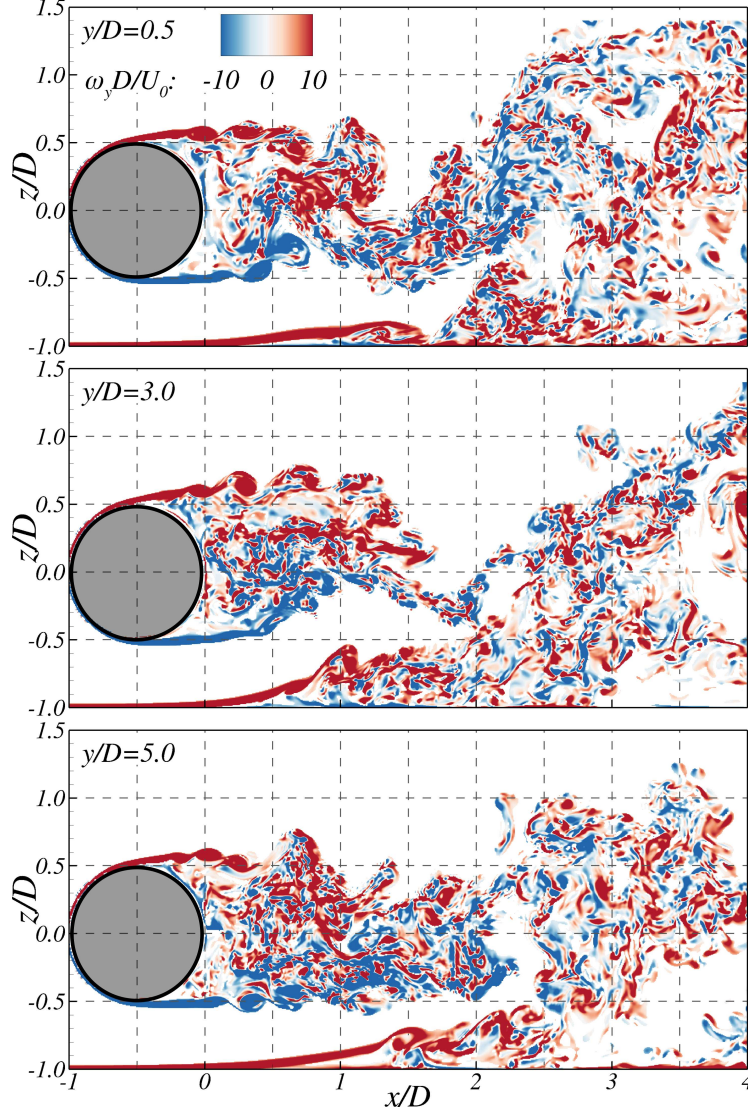


FIG. 12: Contours of normalised spanwise vorticity at three different spanwise locations across the cylinder for the  $Re = 6,666$  and  $G/D = 0.5$  case. Flow is from left to right.

and interacting with the vortical structure generated behind the cylinder, constraining the formation of the lower roller while pairing with the energetic structures, i.e. von-Kármán vortices, of oppositely signed vorticity as it is convected downstream to form a single vortical structure after  $x/D > 2$ .

This complex GV-cylinder wake interaction occurs at  $G/D = 0.5$  for all three Reynolds numbers analysed and is very similar to those found at lower  $Re$  in previous studies<sup>3,16</sup>. However, it is more pronounced for the highest Reynolds number case as the near-wake becomes more unstable, thus leaving more space for the GV to develop. Conversely, increasing

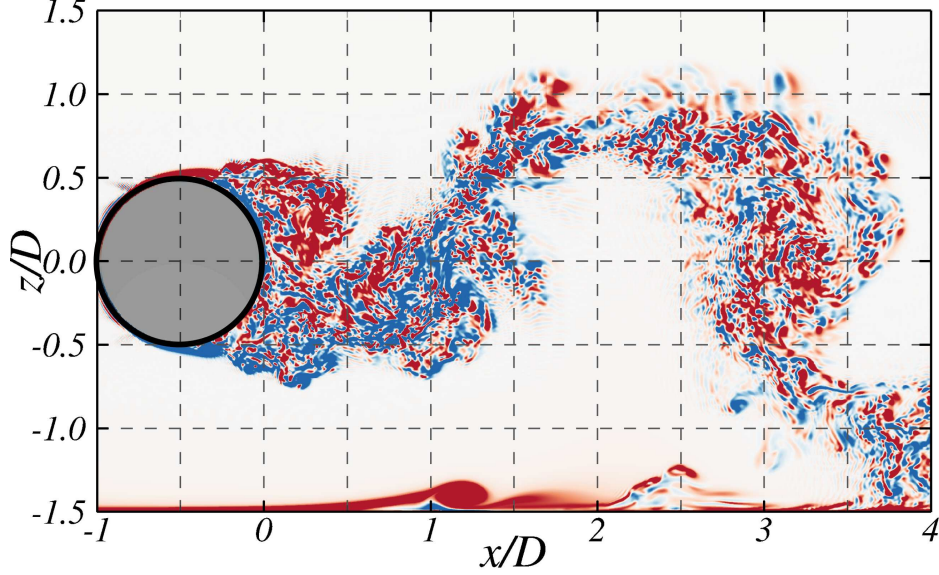


FIG. 13: Contours of normalised spanwise vorticity at a plane at  $y/D = 3.0$  for the  $Re = 13,333$  and  $G/D = 1.0$  case. Flow is from left to right. Same colour range as in Fig. 12.

the gap ratio to 1.0 leads to a notable reduction in the instantaneous cylinder flow dynamics attributable to proximity to the bottom wall. Fig. 13 shows spanwise vorticity contours for  $Re = 13,333$  at  $y/D = 3.0$  in which the GV appears but has no effect on the generation of the von-Kármán vortices immediately behind the cylinder. Increasing the gap ratio reduces flow acceleration close to the ground, which leads to a more uniform GV in the spanwise direction, contrary to its changing shape for  $G/D = 0.5$  shown in Fig. 12. Further details on the generation of the GV are discussed in Section V.

This ground-effect phenomenon has previously been observed in experimental studies<sup>1,2,16,21</sup> and motivated computational analyses using Reynolds Averaged Navier-Stokes<sup>17</sup>, Detached-Eddy Simulation<sup>26</sup>, LES<sup>3</sup> and DNS in the laminar regime<sup>18,19</sup>. The gap-to-diameter ratio ( $G/D$ ) setup of 0.5 corresponds to the intermediate gap regime which relates the influence of the ground-effect on the cylinder's near-wake structure, and more specifically regulates whether large-scale von-Kármán vortices are shed or not<sup>1,2</sup>. For  $G/D = 0.5$ , the ground influence is relatively small allowing the large-scale vortices to be shed but their active interaction with each other, as shown in Fig. 12, is in contrast to unbounded cylinder flows.

Prasad and Williamson<sup>45</sup> described two main of intermittent secondary instabilities developed in the shear layers and roll-up vortices in addition to the classic primary instability which is the shedding of von-Kármán vortices. Two main secondary instabilities

474 modes can be found in the cylinder flow in the sub-critical regime: mode A resulting from  
 475 the vortex dislocations in narrow spatial regions, also referred to as ‘3D instability’, and  
 476 mode B as an oblique convection of the KH vortices during their early shedding, i.e. be-  
 477 fore rolling up to von-Kármán vortices, known as ‘quasi-2D instability’<sup>47</sup>. Both modes  
 478 appear in the present cases. Fig. 14 shows the top-view of iso-surfaces of normalised  $Q$ -  
 479 criterion<sup>48</sup> ( $Q^* = QD^2/U_0^2 = 21$ ) coloured with relative elevation  $z/D$  for the  $Re = 13,333$   
 480 case and  $G/D = 0.5$ .

481 The Kelvin-Helmholtz instability developed by the transition of shear layers coming off  
 482 the edge of the cylinder to smaller rollers is shown to occur closer to the cylinder’s wall  
 483 for the  $Re = 13,333$  case than the  $Re = 6,666$  case. Thereafter, in the near-wake region  
 484 spanwise rollers are formed with an undulating shape instead of being parallel to the cylin-  
 485 der edge (as marked with dotted line in Fig. 14), which exhibits a wavelength  $\lambda$  of approx.  
 486  $\pi D/2$ , in agreement with the findings from Braza et al.<sup>49</sup> who quantified that this wavelength  
 487 can vary from  $3.0$ – $4.5D$ . Interestingly, vortex discontinuities caused by the large-scale von-  
 488 Kármán vortices are irregularly distributed across the whole spanwise length, as mode A  
 489 instabilities<sup>47</sup>. There is some correlation between the undulated spanwise roller and vortices  
 490 dislocations<sup>13</sup>, as those dislocations found at  $y/D \approx 3.8$  or  $1.0$  are located further down-  
 491 stream in-line with low-momentum regions developed in the downstream roller at  $x/D \approx 1$ .  
 492 At the time instance shown in Fig. 14, the large-scale structures at elevations  $z/D > 1$  found  
 493 between  $3 < x/D < 5$  are convected downstream in an oblique manner, i.e. with an angle  
 494 relative to the cylinder edge. This is a well-known feature of the far-wake in cylinder flows<sup>13</sup>  
 495 and interestingly occurs in the present case even though the flow is laterally constrained by  
 496 the flume sidewalls, which also induce flow separation although its effect on the main wake  
 497 structure is thought to be minimal.

498 Fig. 15 gives further insight into the instantaneous vortex shedding for the  $Re = 13,333$   
 499 and  $G/D = 0.5$  case with iso-surfaces of pressure fluctuation ( $p' = p - \langle p \rangle$ ) and  $Q$ -criterion  
 500 at time instants every  $T/6$ , where  $T = 1/f_p$ ,  $T$  and  $f_p$  being the vortex shedding period and  
 501 frequency, respectively. Fig. 15a depicts the roller  $R_1$  coming off the upper surface of the  
 502 cylinder is somewhat coherent over the spanwise direction as a unique structure and features  
 503 an undulating or wavy shape and sheds in a slightly oblique manner as mode B instability.  
 504 Shortly after, at  $2T/6$  (Fig. 15b), at  $x/D = 1.0$  the roller  $R_1$  develops a discontinuity,  $D_1$ ,  
 505 and is divided into main two finite spanwise long rollers that are convected downstream



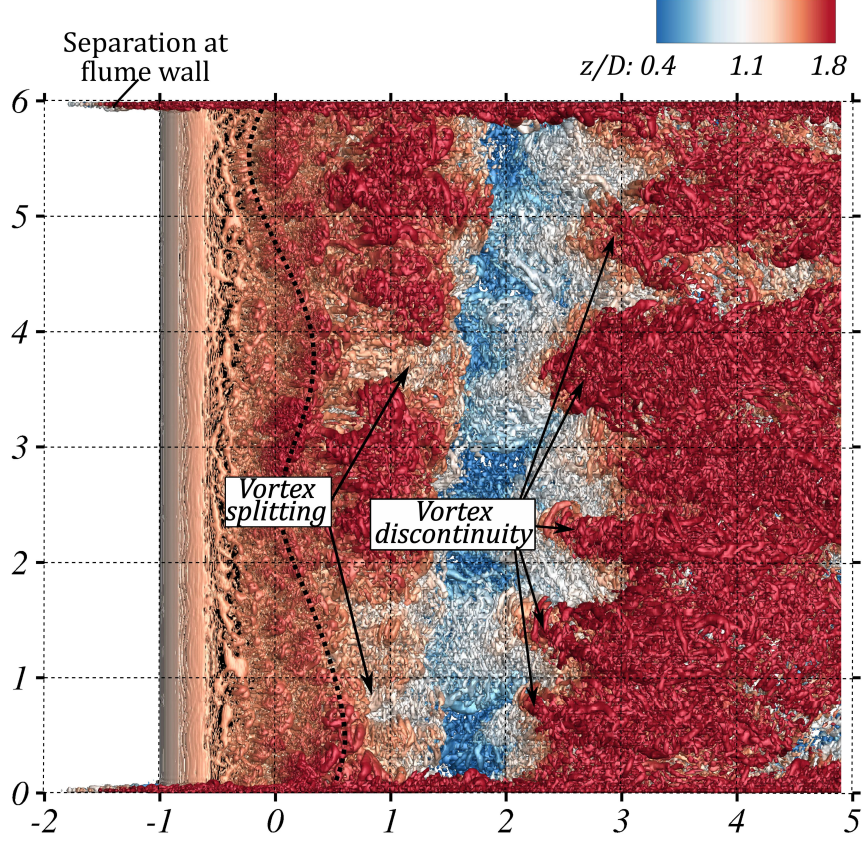


FIG. 14: Top-view of iso-surfaces of  $Q$ -criterion ( $Q^* = QD^2/U_0^2 = 21$ ) coloured by the relative elevation  $z/D$  for the  $Re = 13,333$  case and  $G/D = 0.5$ . Arrows indicate the location of the vortex discontinuities. Flow is from left to right.

506 with the mean flow and whose size increases at the next time instant  $3T/6$ . This sequence  
 507 is analogous to the vortex splitting identified in Fig. 14. At  $x/D = 2$  (Fig. 15d), the rollers  
 508 start to feature smaller scale, localised instabilities as a result of their interaction with the  
 509 turbulent flow going over the cylinder, which is linked to mode A instabilities. These small  
 510 scale vortices result from the change in vorticity<sup>49</sup>, which was observed during experiments<sup>50</sup>,  
 511 and grow in size during their downstream convection, as seen in Fig. 15e and f. Note that  
 512 despite these turbulent structures originating with the roller, they appear to be connected  
 513 to the vortical structures shed from the bottom half of the cylinder, as shown in Fig. 12 in  
 514 the far wake region at  $x/D > 2$ . Instantaneous flow structures in Fig. 15g, h and i capture  
 515 the formation of a new roller,  $R_2$ , that is again shed obliquely to the transverse direction  
 516 similarly to previous experimental observations<sup>45</sup>. Interestingly, this roller again features a  
 517 dislocation  $D_2$  but at a different spanwise location to that shown in Fig. 15a, identifying



518 the intermittent nature of the shear layer breakdown.

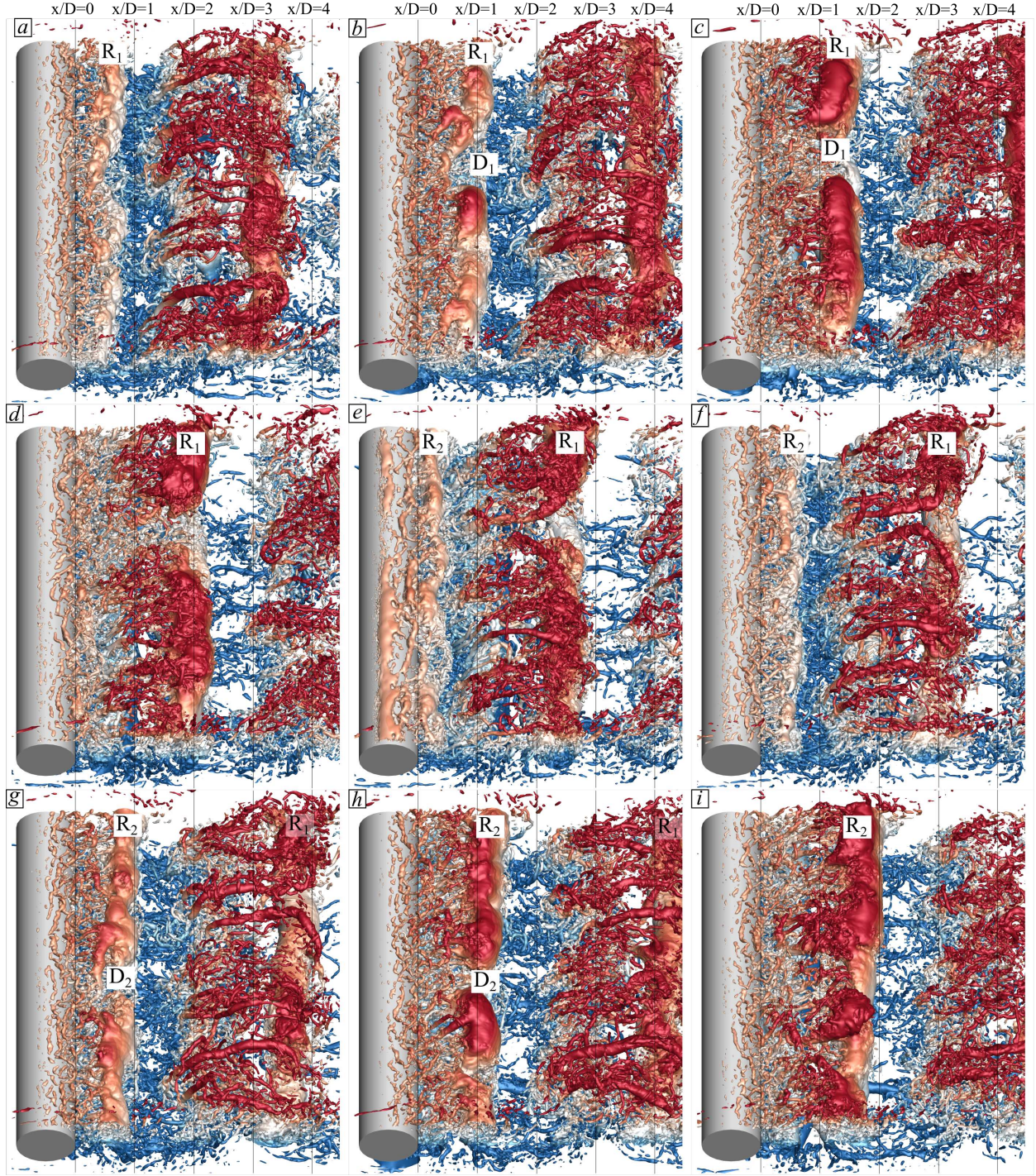


FIG. 15: Snapshots of iso-surfaces of instantaneous pressure fluctuation,  $p'$ , and  $Q$ -criterion coloured with vertical elevation (see contour label in Fig. 14) for the  $Re = 13,333$  and  $G/D = 0.5$  case. An interval of  $T/6$ , with  $T$  being the vortex shedding period, is kept between snapshots. Flow is from left to right.

## F. Dominant shedding frequency and hydrodynamic coefficients

The hydrodynamic forces generated on the cylinder are impacted by the asymmetric flow field developed around the cylinder owing to both its proximity to the bed and the upstream velocity logarithmic distribution. The cylinder forces are directly calculated from the immersed boundary method<sup>36</sup> in the horizontal and vertical directions,  $F_x$  and  $F_z$  respectively, and are used to calculate the drag ( $C_D$ ) and lift ( $C_L$ ) coefficients given by:

$$C_D = \frac{F_x}{1/2\rho AU_0^2} \quad (6)$$

$$C_L = \frac{F_y}{1/2\rho AU_0^2} \quad (7)$$

where  $\rho$  is the fluid density and  $A$  is the cylinder's cross-sectional area. Values of the time-averaged hydrodynamic coefficients and their root-mean-square (*rms*) values are presented in Table IV. The drag coefficient decreases with increasing Reynolds number, with values considerably lower than those found in unbounded cylinder flows due the proximity of the cylinder to the bed<sup>21,23</sup>, and the shallow flow conditions that increase the relative flow blockage of the cylinder. Time-averaged fluctuations of  $C_D$  for  $G/D = 0.5$  are similar for the  $Re = 6,666$  and  $10,000$  cases but decrease for the highest Reynolds number case ( $Re = 13,333$ ), the same trend is present for  $G/D = 1.0$ . The ground-effect is responsible for the upwards force with time-averaged  $C_L$  values ranging from  $0.014$ – $0.017$  for  $G/D = 0.5$ , whilst similar  $\overline{C_L}$  magnitudes are present for  $G/D = 1.0$  as the force now acts in a downward direction. This is a consequence of the cylinder being immersed in the boundary-layer inflow, leading to a higher momentum flowing over the cylinder than beneath it<sup>22</sup>. The time-averaged fluctuations of the  $C_L$  are more than double the magnitude for the  $G/D = 0.5$  than for the  $G/D = 1.0$  due to the ground-effect. For both gap ratio cases, the  $rms(C_L)$  values increase with increasing Reynolds number.

Figure 16 presents the Power Spectral Distribution (PSD) of the vertical forces ( $F_z$ ) experienced by the cylinder under the flow conditions considered with gap ratios  $1.0$  and  $0.5$ . For each geometry configuration, energy peaks collapse into Strouhal numbers ( $St = f_p D/U_0$ ) between  $0.257$  and  $0.307$ , summarised in Table IV, with values for  $G/D = 1.0$  constantly smaller than those with a narrower gap ratio<sup>24</sup>. In the former configuration, the  $St$  are closer to those attained in unbounded cylinder flows, i.e.  $St \approx 0.21$ <sup>15</sup>, due to a reduced influence of



TABLE IV: Values of time-averaged drag ( $\overline{C_D}$ ) and lift ( $\overline{C_L}$ ) coefficients and their root-mean-square, peak frequencies ( $f_p$ ) and Strouhal number ( $St$ ) obtained in the experiments and LES.

Re	$G/D$	$\overline{C_D}$	$rms(C_D)$	$\overline{C_L}$	$rms(C_L)$	$f_p$ (LES) [ $s^{-1}$ ]	$f_p$ (Exp) [ $s^{-1}$ ]	$St$ (LES)	$St$ (Exp)
6,666	0.5	0.443	0.062	0.014	0.142	0.819	0.85	0.307	0.32
6,666	1.0	0.447	0.059	-0.019	0.059	0.801	-	0.300	-
10,000	0.5	0.414	0.062	0.015	0.155	1.105	1.21	0.276	0.30
10,000	1.0	0.441	0.054	-0.015	0.064	1.087	-	0.271	-
13,333	0.5	0.400	0.059	0.017	0.158	1.490	1.61	0.279	0.30
13,333	1.0	0.424	0.053	-0.014	0.064	1.372	-	0.257	-

proximity to the wall, although these remain slightly higher due to effects from the confined domain. These distinct energy peaks are observed at the vortex shedding peak frequency ( $f_p$ ), which becomes higher with increasing Reynolds number as shown in Table IV. Harmonics of these frequencies observed at  $2f_p$  and  $3f_p$  are more pronounced in the configuration with the cylinder closer to the ground specially for the  $Re = 13,333$  case. Experimental Strouhal values presented in Table IV were obtained from the PSD of the time-history of vertical velocities at the sampling point located at  $x/D = 6$ ,  $z/D = 1.5$  for  $G/D = 0.5$  and these are very close to the values from the simulations. These experimental and LES-modelled results show a slight decline in Strouhal number with increasing Reynolds number which has been observed in lower Reynolds number studies<sup>3,16</sup>. Furthermore, previous experimental tests reported increases in  $St$  as the  $G/D$  ratio decreased with values ranging between 0.18–0.28 with  $G/D = 0.5$  although for lower Reynolds numbers<sup>16,21,24</sup>. It should be noted that the logarithmic distribution of the approaching flow also affects the values of the hydrodynamic forces even for  $G/D = 1.0$ <sup>22,23</sup>, which also explains the present  $St$  values and hydrodynamic coefficients.

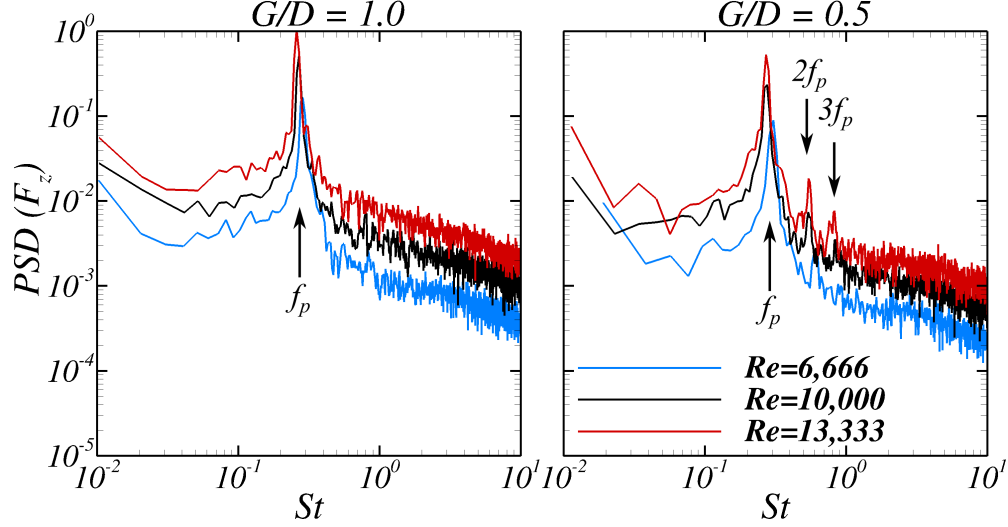


FIG. 16: Spectral energy distribution of the vertical forces ( $F_z$ ) in the cylinder computed from the LES for the three Reynolds number cases studied with gap ratios 1.0 (left) and 0.5 (right).

## V. DISCUSSION ON THE GENERATION OF THE GROUND-VORTEX

To give new insights into the ground-vortex (GV) formation and its lift-up, the main interactions observed in the wake in cylinder flows in proximity of a solid wall with  $G/D = 0.5$  are summarised in Fig. 17, based on the mean and instantaneous wake distribution shown in Fig. 9d and 12, respectively. As the flow approaches the cylinder, it accelerates over its upper and lower sides. For small gap-to-diameter ratios, e.g.  $G/D = 0.5$ , the flow going under the cylinder is accelerated akin to a jet-flow as a result from an adverse pressure gradient, which is larger over the region between the bed and the cylinder's underside<sup>51</sup>. This is supported by the distribution of  $\partial\langle u\rangle/\partial x$  in Fig. 11.

Upon passing the cylinder's underside, there is a favourable pressure gradient and the flow is able to expand vertically<sup>15</sup>. In this region the velocity profile is influenced by the solid cylinder and bottom walls, which induce the flow to exhibit a parabolic velocity profile<sup>52</sup>. Hence, the gradient  $\partial\langle u\rangle/\partial z$  is positive near the bottom and negative in the cylinder's lower shear layer (Fig. 11). The generation of the bottom shear layer due to this velocity gradient can be well-explained by the definition of spanwise vorticity:

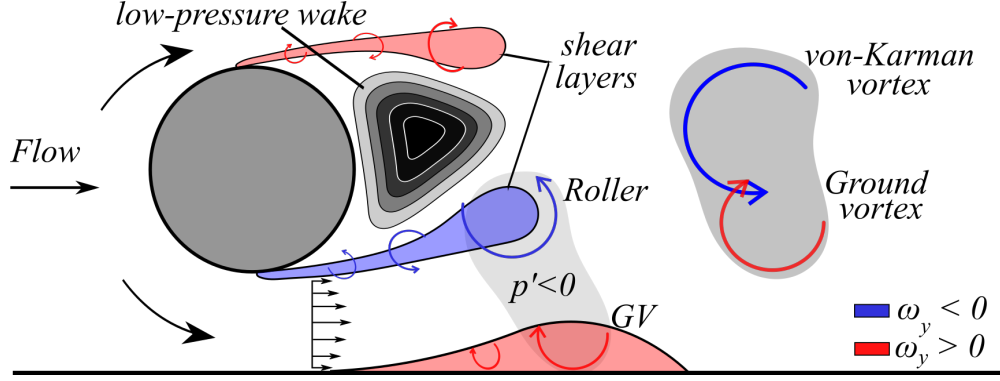


FIG. 17: Schematic of the mechanisms responsible for the appearance and progression of the ground vortex for small gap-to-diameter ratios.

$$\omega_y = \frac{\partial u}{\partial z} - \frac{\partial w}{\partial x} \quad (8)$$

In the contribution to the generation of  $\omega_y$ , the term  $\partial w/\partial x$  is smaller than  $\partial u/\partial z$ , thus the vorticity field near the bottom wall is nearly proportional to the vertical gradient of streamwise velocities of positive sign, as seen in Fig. 9d. As observed in Fig. 12, there is a region of high-vorticity attached to the bottom boundary identifying the bottom shear layer that starts to separate, i.e. increase its thickness, after surpassing the cylinder's lee side at  $x/D = 0$ , as a result of the favourable pressure gradient<sup>15,53</sup>. This explains that, when the bottom boundary moves<sup>1,26</sup> or approach flow boundary layer thickness is relatively small<sup>53</sup>, the bottom shear layer is either attenuated or not formed due to reduced velocity gradients.

To provide further understanding of the bottom shear layer transition and interaction with the cylinder's wake, Fig. 18 presents contours of pressure fluctuation,  $p'$ , together with isolines of spanwise vorticity and flow streamlines at an  $xz$ -plane at  $y/D = 4$  for cases with  $Re = 6,666$  and  $13,333$  with  $G/D = 0.5$ . The flow streamlines allow to visualise the onset of a separation bubble in the bottom shear layer that rolls up, growing in size further downstream. At  $x/D = 1.0$  for both  $Re$  cases, this bubble eventually becomes large enough to generate the GV, as also depicted in Fig. 12a. The cylinder's shear layer becomes unstable rapidly after separation with Kelvin-Helmholtz or roller structures being formed and growing in size with increasing distance downstream.

In the area occupied by the roller ( $R$ ) the values of  $p'$  are negative, where this instantaneous pressure field responsible for the quick GV lift-off, which also exhibits negative

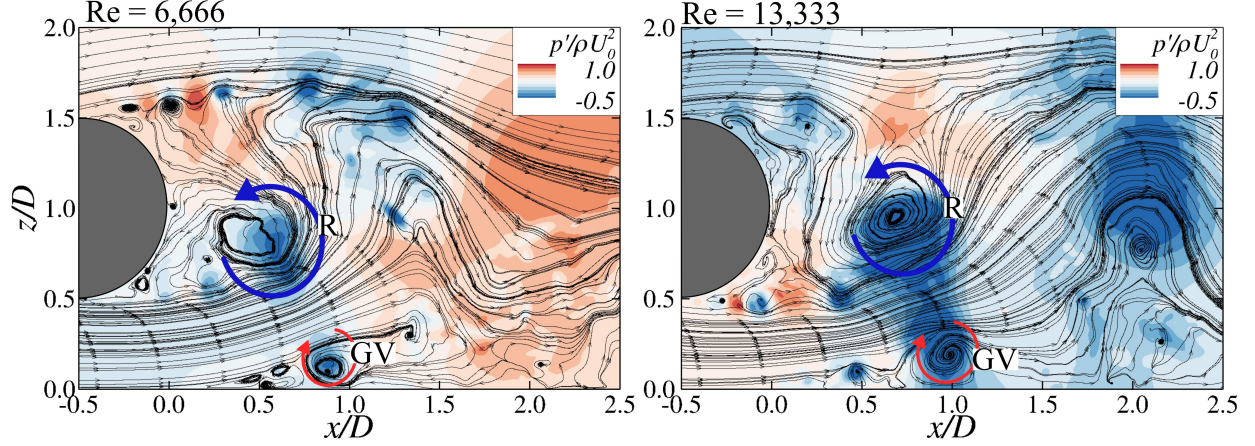


FIG. 18: Contours of normalised pressure fluctuation,  $p'/\rho U_0^2$ , with flow streamlines at a  $xz$ -plane at  $y/D = 4$  for cases with  $Re = 6,666$  (left) and  $13,333$  (right) with  $G/D = 0.5$ .

values of pressure fluctuation. This R-GV coupling is observed for both Reynolds numbers whilst been more obvious in the  $Re = 13,333$ . The mechanisms driving the near-wall flow transition, separation and instabilities is somewhat similar to those in flows over flat plate under adverse pressure gradient boundary layers but, in this case, the cylinder-shed vortical structures trigger suction areas, i.e. of negative pressure, causing the lift-off of the GV to occur relatively close to the cylinder. These observations agree very well with experimental visualisations from Bearman and Zdravkovich<sup>15</sup> and Grass et al.<sup>53</sup>. Finally, it is worth to mention that the GV has a clockwise rotation whilst the cylinder's shear layer rollers have an opposite rotational direction. Thus, once both structures merge and are shed, they form the von-Kármán vortex that is convected downstream with the flow, as observed at  $x/D = 2.0$  for the  $Re = 13,333$  case, but whose expected clear counter-clockwise motion is damped as result of the GV.

To better explain the detachment of the bottom shear layer off the bottom wall, Fig. 19 presents contours of spanwise vorticity at five horizontal planes at elevations  $z/H$  in the range of 0.00667–0.060 for  $Re = 6,666$  and  $13,333$  with  $G/D = 0.5$ . At the plane closest to the bottom, it is seen that the transition from the wall shear layer to the separated bubble is accomplished after  $x/D = 0$ , being more subtle for the lower  $Re$ . However, it is appreciated that the location of the transition point is heterogeneous in the spanwise direction, resulting from its intermittent motion upstream and downstream analogously to the cylinder's shear layer. It is also observed that the lateral walls induce flow separation and hence play are

role in the transition of the bottom laminar shear layer to the GV formation at the ends of  
the domain.

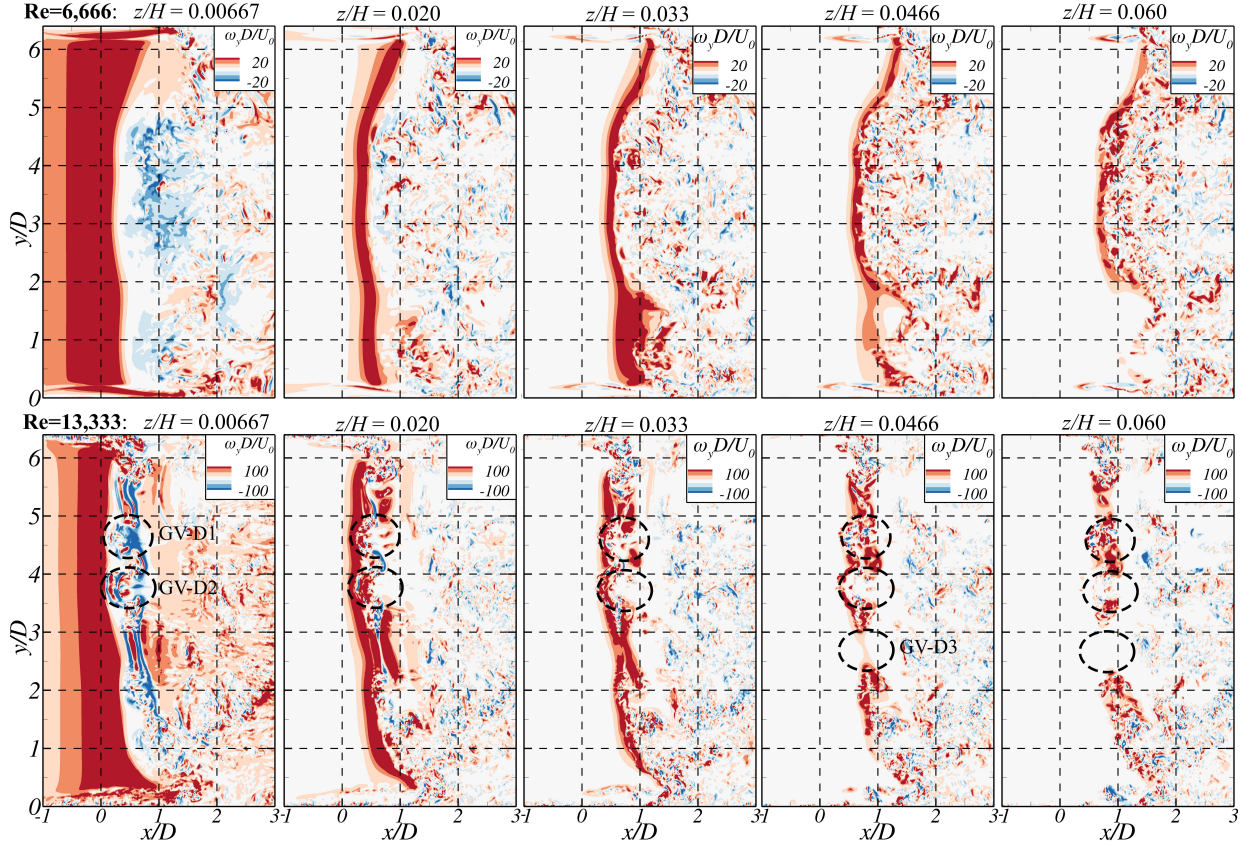


FIG. 19: Contours of spanwise vorticity at elevations  $z/H = 0.00667, 0.020, 0.033, 0.0466$  and  $0.060$  for the cases with  $Re = 6,666$  (top) and  $13,333$  (bottom), and  $G/D = 0.5$ .

Comparing the vorticity distribution for both  $Re$ , it is clear that in this near-wall region  
the flow separation phenomena depends on the Reynolds number. At  $Re = 13,333$ , three  
vortex dislocations are developed, similar to those mode A instabilities found in the cylinder  
shear layers, with two of them,  $GV-D1$  and  $D2$ , already found near the bottom wall at  $z/H$   
 $= 0.00667$  whilst  $GV-D3$  is observed at elevations above  $z/H = 0.0466$ . Fig. 19 allows to  
observe that the GV, at an elevation  $z/H = 0.060$  for  $Re = 6,666$ , features some spatial  
coherence as a long roller of high-vorticity spanning between  $2 < y/D < 5$  at  $x/D \approx 0.5$ ,  
whilst for the higher Reynolds number discontinuities in the GV are observed at  $z/H =$   
 $0.0466$ .

For cases with  $G/D = 1.0$  the mechanisms responsible for connecting and merging the  
R and GV are almost negligible as seen in Fig. 13. Increasing the distance between the



cylinder and the wall reduces the negative pressure fluctuations and their impact on the roller R interference with the GV formation and subsequent lift off. Planviews of spanwise vorticity near the bed show that the GV is fairly uniform across the domain length (not shown here for brevity). The bottom wall affects the far-wake for the larger gap ratio in that the von-Kármán vortices impingement on the ground constrains their vertical expansion. Hence, the near-wake dynamics developed behind the cylinder with  $G/D = 1.0$  are similar to those in unconfined cylinder flows, whilst the far-wake can slightly differ due to the limited freedom of the large-scale vortices to move vertically in their downstream convection.

## VI. CONCLUSIONS

The nature of the turbulent wake behind a circular cylinder in close proximity to a solid boundary have been investigated using a combined experimental and large-eddy simulation study for Reynolds numbers in the range 6,666 to 13,333 with gap-to-diameter ratios of 0.5 and 1.0. The LES results agreed well with the experimental measurements for the time-averaged flow quantities and captured the streamwise velocity, its fluctuation in the circulation bubble, and the upward flow motion. The presence of a narrow gap between the wall and cylinder, at a ratio of 0.5, significantly influenced the dynamics of the vortex generation and shedding which, in consequence, led to an increasingly pronounced asymmetric wake distribution with increasing Reynolds number. The boundary layer separation points on both the upper and lower halves of the cylinder move upstream with increasing Reynolds number, which is consistent with previous studies. Likewise, the enclosed recirculation bubble, was found to be slightly asymmetric by being larger in its lower part and decreasing in longitudinal extent with increasing Reynolds number consistently with cylinder-wake flows. This impact on the wake asymmetry reduced for cases with gap ratio of 1.0. From the continuity equation, the rate of change of the mean velocity terms further characterised the asymmetric near-wake in the cases with the cylinder close to the ground, whose distribution was similar for the three Reynolds numbers.

The Kelvin-Helmholtz instabilities developed in the upper and lower shear layers were shown to be decoupled in that these shear layers followed a laminar-to-turbulent transition at different downstream distances. A more rapid breakdown of the shear layers occurred for the  $Re = 13,333$  case than the  $Re = 6,666$  case. In the near-wake region spanwise rollers

were formed with an undulating pattern instead of being parallel to the cylinder edge, which was linked to the appearance of vortex dislocations. The ground-vortex formed as a result of the lower vortex inducing a difference in pressure near the bottom wall which allowed the former structure to lift-off the ground and merge with the von-Kármán vortices to form a single vortical structure. This phenomenon was present for all three Reynolds numbers examined for the gap ratio of 0.5, and became more pronounced for the highest Reynolds number case as the near wake became more unstable closer to the cylinder.

Spectral analysis revealed Strouhal numbers varied between 0.28-0.32 for the gap ratio of 0.5 for both the experiments and LES whilst varied in the range of 0.25–0.30 for the gap ratio of 1.0. For all these scenarios, the Strouhal numbers remain higher than the value of 0.21 commonly found for unbounded cylinder flows owing to changes in the vortex shedding dynamics from the ground-effect. In this line, drag coefficients increased when the gap between the cylinder and the ground was greater whilst remaining lower than those for unbounded cylinder flows. An upwards force was present on the cylinder for the gap ratio of 0.5, due to the proximity to the bottom boundary, while a mean vertical downforce was present for the case with larger gap ratio owed to the boundary layer flow carrying more momentum over the cylinder than below it.

## **Appendix A: Time-averaged flow hydrodynamics for the $Re = 13,333$ and $G/D = 0.5$ case.**

The influence of the Reynolds number in the wake behind the cylinder in proximity to the wall with  $G/D = 0.5$  is presented in Fig. 20 for  $Re = 13,333$ .

## **ACKNOWLEDGMENTS**

The authors would like to acknowledge the support of the Supercomputing Wales project, which is part-funded by the European Regional Development Fund (ERDF) via the Welsh Government.

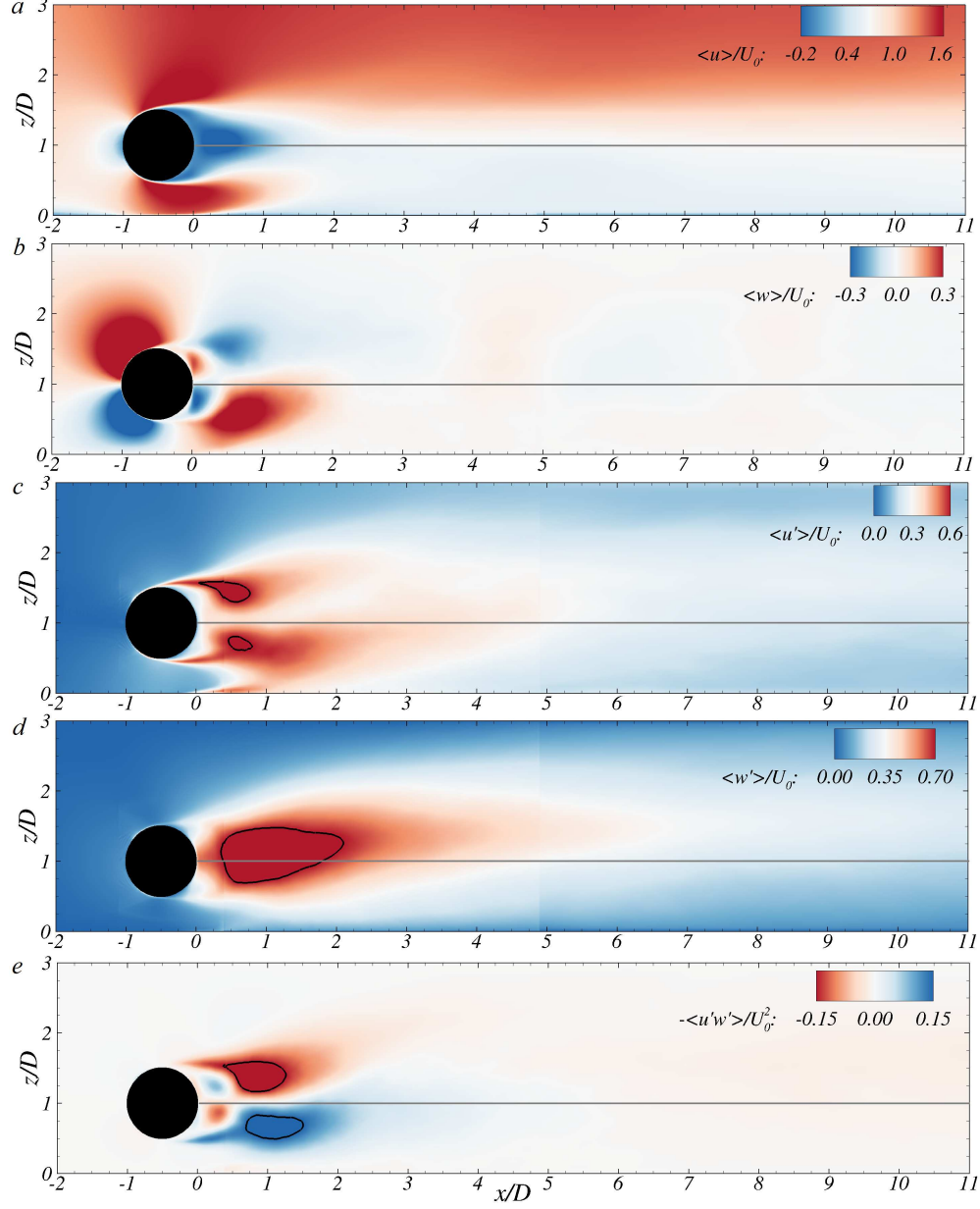


FIG. 20: Side elevation contour plots of the LES computed (a) streamwise velocity, (b) vertical velocity, (c) streamwise turbulence intensity with lines denoting  $\langle u' \rangle / U_0 = 0.6$ , (d) vertical turbulence intensity with lines denoting  $\langle w' \rangle / U_0 = 0.7$ , and (e) Reynolds shear stress with the solid lines corresponding to  $\langle u'w' \rangle / U_0^2 = \pm 0.1$ , normalised by the bulk velocity for the  $Re = 13,333$  and  $G/D = 0.5$  case.

## REFERENCES

- <sup>1</sup>T. Nishino, G. T. Roberts, and X. Zhang, “Vortex shedding from a circular cylinder near a moving ground,” *Physics of Fluids* **19**, 025103 (2007).

- <sup>2</sup>A. Oner, M. Kirkgoz, and M. Akoz, “Interaction of a current with a circular cylinder near a rigid bed,” *Ocean Engineering* **35**, 1492–1504 (2008).
- <sup>3</sup>S. Sankar and S. Sankar, “ Vortex dynamics of a cylinder wake in proximity to a wall,” *Journal of Fluids and Structures* **26**, 19–40 (2010).
- <sup>4</sup>M. Unal and D. Rockwell, “On vortex shedding from a cylinder: Part 1. The initial instability,” *Journal of Fluid Mechanics* **174**, 113 (1988).
- <sup>5</sup>C. Chyu, J. Lin, J. Sheridan, and D. Rockwell, “Karman vortex formation from a cylinder: Role of phase-locked Kelvin–Helmholtz vortices,” *Physics of Fluids* **7**, 2288–2290 (1995).
- <sup>6</sup>O. Lehmkuhl, I. Rodriguez, R. Borrell, and A. Oliva, “Low-frequency unsteadiness in the vortex formation region of a circular cylinder,” *Physics of Fluids* **25**, 085109 (2013).
- <sup>7</sup>D. Aljure, O. Lehmkuhl, I. Rodriguez, and A. Oliva, “Three dimensionality in the wake of the flow around a circular cylinder at Reynolds number 5000 ,” *Comput. Fluids* **147**, 102–118 (2017).
- <sup>8</sup>A. Prasad and C. H. Williamson, “The instability of the separated shear layer from a bluff body,” *Physics of Fluids* **8**, 1347 (1996).
- <sup>9</sup>C. Norberg, “An experimental investigation of the flow around a circular cylinder: influence of aspect ratio,” *Journal of Fluid Mechanics* **258**, 287–316 (1994).
- <sup>10</sup>C. Wieselsberger, “Neuere feststellungen uber die gesetze des flussigkeits und luftwiderstands,” *Phys. Z.* **22**, 321 (1921).
- <sup>11</sup>A. Roshko, “Experiments on the flow past a circular cylinder at very high Reynolds number,” *Journal of Fluid Mechanics* **10**, 345–356 (1961).
- <sup>12</sup>O. Lehmkuhl, I. Rodriguez, R. Borrell, J. Chiva, and A. Oliva, “Unsteady forces on a circular cylinder at critical Reynolds numbers,” *Physics of Fluids* **26**, 125110 (2014).
- <sup>13</sup>C. Williamson, “Vortex dynamics in the cylinder wake,” *Annu. Rev. Fluid. Mech* **28**, 477–539 (1996).
- <sup>14</sup>D. Sumner, “Flow above the free end of a surface-mounted finite-height circular cylinder: A review,” *J Fluids and Structures* **43**, 41–63 (2013).
- <sup>15</sup>P. Bearman and M. Zdravkovich, “Flow around a circular cylinder near a plane boundary,” *Journal of Fluid Mechanics* **89**, 33–47 (1978).
- <sup>16</sup>S. Price, D. Sumner, J. Smith, K. Leong, and M. Paidussis, “Flow visualisation around a circular cylinder near to a plane wall,” *Journal of fluids and structures* **16**, 175–191 (2002).

- <sup>17</sup>M. Kirkgoz, A. Oner, and M. Akoz, “Numerical modeling of interaction of a current with a circular cylinder near a rigid bed,” *Advances in Engineering Software* **40**, 1191–1199 (2009).
- <sup>18</sup>B. E. Stewart, M. C. Thompson, T. Leweke, and K. Hourigan, “The wake behind a cylinder rolling on a wall at varying rotation rates,” *Journal of Fluid Mechanics* **648**, 225–256 (2010).
- <sup>19</sup>A. Rao, M. Thompson, T. Leweke, and K. Hourigan, “The flow past a circular cylinder translating at different heights above a wall,” *Journal of Fluids and Structures* **41**, 9–21 (2013).
- <sup>20</sup>A. Roshko, A. Steinolfson, and V. Chattoorgoon, “Flow Forces on a Cylinder near a Wall or near Another Cylinder,” in *Proceedings of the 2nd US Nation Conference on Wind Engineering Research, Fort Collins, Paper IV-15* (1975).
- <sup>21</sup>J. Choi and S. Lee, “Ground effect of flow around an elliptic cylinder in a turbulent boundary layer,” *Journal of Fluids and Structures* **14**, 697–709 (2000).
- <sup>22</sup>M. Zdravkovich, “Forces on a circular cylinder near a plane wall,” *Applied Ocean Research* **7**, 197–201 (1985).
- <sup>23</sup>C. Lei, L. Cheng, and K. Kavanagh, “Re-examination of the effect of a plane boundary on force and vortex shedding of a circular cylinder,” *Journal of Wind Engineering and Industrial Aerodynamics* **80**, 263–286 (1999).
- <sup>24</sup>F. Angrilli, S. Bergamaschi, and V. Cossalter, “Investigation of Wall Induced Modifications to Vortex Shedding From a Circular Cylinder,” *Journal of Fluids Engineering* **104**, 518–522 (1982).
- <sup>25</sup>S. Taniguchi and K. Miyakoshi, “Fluctuating fluid forces acting on a circular cylinder and interference with a plane wall,” *Experiments in Fluids* **9**, 197–204 (1990).
- <sup>26</sup>T. Nishino, G. T. Roberts, and X. Zhang, “Unsteady RANS and detached-eddy simulations of flow around a circular cylinder in ground effect,” *Journal of Fluids and Structures* **24**, 18–33 (2008).
- <sup>27</sup>M. Breuer, “Large eddy simulations of the subcritical flow past a circular cylinder: numerical and modeling aspects,” *International Journal for Numerical Methods in Fluids* **28**, 1281–1302 (1998).
- <sup>28</sup>X. Ma, G.-S. Karamanos, and G. E. Karniadakis, “Dynamics and low-dimensionality of a turbulent near wake,” *Journal of Fluid Mechanics* **410**, 29–65 (2000).

- <sup>29</sup>D. Goring and V. Nikora, “Despiking Acoustic Doppler Velocimeter Data,” *J. Hydraul. Eng* **128**, 117–126 (2002).
- <sup>30</sup>M. Jesson, M. Sterling, and J. Bridgman, “Despiking velocity time-series—Optimisation through the combination of spike detection and replacement methods,” *Flow Measurement and Instrumentation* **30**, 45–51 (2013).
- <sup>31</sup>L. Cea, J. Puertas, and L. Pena, “Velocity measurements on highly turbulent free surface flow using ADV,” *Experiments in Fluids* **42**, 333–348 (2007).
- <sup>32</sup>T. Stoesser, S. Kim, and P. Diplas, “Turbulent Flow through Idealized Emergent Vegetation,” *J. Hydraul. Res.* **136**, 1003–1017 (2010).
- <sup>33</sup>S. Bomminayuni and T. Stoesser, “Turbulence Statistics in an Open-Channel Flow over a Rough Bed,” *J. Hydraul. Eng.* **137**, 1347–1358 (2011).
- <sup>34</sup>D. Kim, T. Stoesser, and J. Kim, “The effect of baffle spacing on hydrodynamics and solute transport in serpentine contact tanks,” *Journal of Hydraulic Research* **51**, 558–568 (2013).
- <sup>35</sup>S. Kara, T. Stoesser, T. W. Sturm, and S. Mulahasan, “Flow dynamics through a submerged bridge opening with overtopping,” *J. Hydraul. Res.* **53**, 186–195 (2015).
- <sup>36</sup>P. Ouro, C. Wilson, P. Evans, and A. Angeloudis, “Large-eddy simulation of shallow turbulent wakes behind a conical island,” *Physics of Fluids* **29**, 126601 (2017).
- <sup>37</sup>R. McSherry, K. Chua, T. Stoesser, and S. Mulahasan, “Free surface flow over square bars at intermediate relative submergence,” *Journal of Hydraulic Research* **1686**, 1–19 (2018).
- <sup>38</sup>F. Nicoud and F. Ducros, “Subgrid-scale stress modelling based on the square of the velocity gradient tensor,” *Flow, Turbulence and Combustion* **62**, 183–200 (1999).
- <sup>39</sup>M. Uhlmann, “An immersed boundary method with direct forcing for the simulation of particulate flows,” *J. Comput. Phys.* **209**, 448–476 (2005).
- <sup>40</sup>P. Ouro and T. Stoesser, “An immersed boundary-based large-eddy simulation approach to predict the performance of vertical axis tidal turbines,” *Computers and Fluids* **152**, 74–87 (2017).
- <sup>41</sup>P. Ouro, B. Fraga, U. López-Novoa, and T. Stoesser, “Scalability of an Eulerian-Lagrangian large-eddy simulation solver with hybrid MPI/OpenMP parallelisations,” *Computers and Fluids* **179**, 123–136 (2019).
- <sup>42</sup>M. Cevheri, R. McSherry, and T. Stoesser, “A local mesh refinement approach for large-eddy simulations of turbulent flows,” *International Journal for Numerical Methods in*

781 Fluids **82**, 261–285 (2016).

782 <sup>43</sup>T. Stoesser, “Large-eddy simulation in hydraulics: Quo Vadis?” J. Hydraul. Res. **52**, 441–  
783 452 (2014).

784 <sup>44</sup>R. Broglia, A. Pascarelli, and U. Piomelli, “Large-eddy simulations of ducts with a free-  
785 surface,” Journal of Fluid Mechanics **484**, 223–253 (2003).

786 <sup>45</sup>A. Prasad and C. H. Williamson, “The instability of the shear layer separating from a  
787 bluff body,” Journal of Fluid Mechanics **333**, 375–402 (1997).

788 <sup>46</sup>M. Rai, “A computational investigation of the instability of the detached shear layers in  
789 the wake of a circular cylinder,” Journal of Fluid Mechanics **659**, 375–404 (2000).

790 <sup>47</sup>J. Kim and H. Choi, “Instability of the shear layer separating from a circular cylinder,”  
791 in *Proceedings of the Third AFOSR International Conference on DNS/LES* (2001).

792 <sup>48</sup>J. Hunt, A. Wray, and P. Moin, “Eddies, streams, and convergence zone in turbulent  
793 flows,” Tech. Rep. (1988).

794 <sup>49</sup>M. Braza, D. Faghani, and H. Persillon, “Successive stages and the role of natural vortex  
795 dislocations in three-dimensional wake transition,” Journal of Fluid Mechanics **439**, 1–41  
796 (2001).

797 <sup>50</sup>C. Norberg, “Pressure forces on a circular cylinder in cross flow,” in *IUTAM symposium:*  
798 *bluff body wakes, dynamics and instabilities, Goettingen, Germany* (1992).

799 <sup>51</sup>Y.-M. Chiew, “Flow Around Horizontal Circular Cylinder in Shallow Flows,” Journal of  
800 Waterway, Port, Coastal, and Ocean Engineering **117**, 25657 (1991).

801 <sup>52</sup>H. Jiang, L. Cheng, S. Draper, and H. An, “Two- and three-dimensional instabilities in  
802 the wake of a circular cylidner near a moving wall,” Journal of Fluids Mechanics **812**,  
803 435–462 (2017).

804 <sup>53</sup>A. Grass, P. Raven, R. Stuart, and J. Bray, “The Influence of Boundary Layer Velocity  
805 Gradients and Bed Proximity on Vortex Shedding From Free Spanning Pipelines,” J.  
806 Energy Resour. Technol. **106**, 70–78 (1984).